arXiv:astro-ph/0603441v2 8 May 2006

DETECTION RATE ESTIMATES OF GRAVITY-WAVES EMITTED DURING PARABOLIC ENCOUNTERS OF STELLAR BLACK HOLES IN GLOBULAR CLUSTERS

BENCE KOCSIS
Institute of Physics, Eötvös University, Pázmány P. s. 1/A, 1117 Budapest, Hungary; bkocsis@complex.elte.hu

MERSE ELŐD GÁSPÁR
Institute of Physics, Eötvös University, Pázmány P. s. 1/A, 1117 Budapest, Hungary; merse@complex.elte.hu

SZABOLCS MÁRKA
Department of Physics, Columbia University, 550 West 120th Street, New York, NY 10027; smarka@phys.columbia.edu
Accepted for publication in ApJ

ABSTRACT

The rapid advance of gravitational-wave (GW) detector facilities makes it very important to estimate the event rates of possible detection candidates. We consider an additional possibility of GW bursts produced during unbound orbits of stellar mass compact objects. We estimate the rate of successful detections for specific detectors: the initial Laser Interferometric Gravitational-Wave Observatory (InLIGO), the French-Italian gravitational-wave antenna VIRGO, the near-future Advanced-LIGO (AdLIGO), the space-based *Laser Interferometric Space Antenna* (*LISA*), and the *Next Generation LISA* (*NGLISA*). The dominant contribution among unbound orbits that have GW frequencies in the sensitive band of the detectors correspond to near-parabolic encounters (PEs) within globular clusters (GCs). Simple GC models are constructed to account for the compact object mass function, mass segregation, number density distribution, and velocity distribution. We calculate encounters both classically and account for general relativistic corrections by extrapolating the results for infinite mass ratios. We also include the cosmological redshift of waveforms and event rates. We find that typical PEs with masses $m_1 = m_2 = 40 M_\odot$ are detectable with matched filtering over a signal to noise ratio $S/N = 5$ within a distance $d_L \sim 200 \, \mathrm{Mpc}$ for InLIGO and VIRGO, $z = 1$ for AdLIGO, $0.4 \, \mathrm{Mpc}$ for *LISA*, and $1 \, \mathrm{Gpc}$ for *NGLISA*. We estimate single datastream detection rates of $5.5 \times 10^{-5} \, \mathrm{yr}^{-1}$ for InLIGO, $7.2 \times 10^{-5} \, \mathrm{yr}^{-1}$ for VIRGO, $0.063 \, \mathrm{yr}^{-1}$ for AdLIGO, $2.9 \times 10^{-6} \, \mathrm{yr}^{-1}$ for *LISA*, and $1.0 \, \mathrm{yr}^{-1}$ for *NGLISA*, for reasonably conservative assumptions. These estimates are subject to uncertainties in the GC parameters, most importantly the total number and mass-distribution of black holes (BHs) in the cluster core. In reasonably optimistic cases, we get $\gtrsim 1$ detections for AdLIGO per year. We can expect that a coincident analysis using multiple detectors and accounting for GW recoil capture significantly increases the detection rates. We give ready-to-use formulas to recalculate the estimates when these input parameters become better-determined. In addition, we provide the partial detection rates for various masses. The regular detection of GWs during PEs would provide a unique observational probe for constraining the stellar BH mass function of dense clusters.

Subject headings: gravitational waves – black holes – globular clusters: general

1. INTRODUCTION

Interferometric gravitational-wave (GW) detectors LIGO, GEO, TAMA, and VIRGO are searching for GW signals with unprecedented sensitivity (Hughes et al. 2001; LIGO Scientific Collaboration 2005a; Abbott et. al. 2005a,b; Grote et al. 2005; Ando et al. 2005; Acernese et al. 2005). For LIGO, the noise levels are already reaching the goal level necessary for the detection of the strongest signals. It is very important to analyze the detection capabilities of these detectors and to estimate the rates of potentially detectable GW signals. There is already a considerable list of possible detection candidates (for a review see Cutler & Thorne 2002): the inspiral of neutron star (NS) or black hole (BH) binaries, the tidal disruption of NS by BH in NS–BH binaries, BH–BH merger and ringdown, low-mass X-ray binaries, pulsars, centrifugally hung-up proto neutron stars in white dwarf accretion-induced collapse, supernova core collapse, gamma ray bursts, and the stochastic background. In this paper we consider an additional possibility, GWs produced by unbound orbits. As we will show, among unbound orbits near-parabolic encounters (PEs) produce gravitational radiation with typical frequencies

appropriate for detection with terrestrial facilities. For close PEs the gravitational radiation is short and intensive, that is observable to large distances. Here, we estimate the expected event rate of detections for specific current and near-future GW detectors.

Initial order-of-magnitude estimates on the detectability of GWs emitted during scattering and near collisions of stellar mass compact objects in active galactic nuclei and globular clusters (GCs) were made by Dymnikova, Popov, & Zentsova (1982). Although their study primarily focused on BH–star, star–star encounters, and did not provide numbers for BH–BH encounters, they identified these encounters to be "quite rare". However, Dymnikova, Popov, & Zentsova (1982) used an overly simplified GC model in which the velocities and masses of all objects were identical, and the spatial distribution was assumed to be homogeneous. We extend the detection rate estimates to account for the stellar BH mass function, mass segregation, and mass-dependent relative velocities. We show that this improvement significantly increases the event rate, by approximately a factor of 10^2. In addition, interferometric GW detector technology has improved greatly

and detailed sensitivity curves are now available. Dymnikova, Popov, & Zentsova (1982) estimated a maximum visible distance of $D_{\max} = 20\,\mathrm{Mpc}$, which is a factor of ~ 100 less than Advanced LIGO's (AdLIGO) capabilities (see Fig. 4 below), i.e. a factor of $\sim 10^6$ less in the accessible volume of sources. Combining these factors, our detection rate estimates yield $\sim 10^8$ times larger results for AdLIGO.

Gravity waves emitted during PEs are also important for creating relativistic orbits by gravitational radiation reaction around the supermassive black holes (SMBH) in the centers of galaxies. The GWs emitted by the later inspiral of the star or compact object around the SMBH are possibly detectable by the future space detector *LISA* (Sigurdsson & Rees 1997; Freitag 2003; Gair et al. 2004) and also by ground-based detectors for highly eccentric orbits (Hopman & Alexander 2005). In the present paper, we do not consider encounters with SMBHs, but focus on the direct detection of GWs from unbound orbits of two stellar mass compact objects (COs).

Stellar mass unbound orbit encounters are expected to be most likely from dense star clusters with a large fraction of COs. Among regular star systems, these features are carried by galactic nuclei and GCs, where central densities reach $10^4 - 10^7\,\mathrm{pc}^{-3}$ within a region of $0.5 - 3\,\mathrm{pc}$ (Pryor & Meylan 1993), the inner regions contain a CO fraction of $q \gtrsim 1/2$ (Sigurdsson & Phinney 1995). In the present paper, we estimate PE event rates for GCs.

As compared to other GW burst sources, the big advantage in detecting PE events is that the possible signal waveforms are much more reliable as the physics behind them is well understood. The waveforms are known analytically for the case of arbitrary masses moving with arbitrary velocities but at small deflection angles (often referred to as gravitational bremsstrahlung, see Kovács & Thorne 1978), arbitrary unbound orbits but low velocities in the Newtonian approximation (Turner 1977), in the post-Newtonian approximation (PN, Blanchet & Schäfer 1989, including corrections $\mathcal{O}(v^2)$), in the 2PN approximation ($\mathcal{O}(v^4)$ Blanchet et al. 1995; Mikóczi, Vasúth, & Gergely 2005), and most recently, in the 3PN approximation (Blanchet et al. 2005, $\mathcal{O}(v^6)$), and the exact numerical solution is available for extreme mass ratios using a Schwarzschild background approximation (Martel 2004), and finally, for head-on collisions with large velocities (D'Eath & Payne 1992). Thus, PE waveforms are available for a very large portion of the parameter space. Waveform templates can be constructed a priori, similar to inspirals. The prior knowledge of the possible waveforms allows the method of matched filtering detection, which helps to reduce the minimum signal-to-noise ratio necessary for a confirmed detection (Flanagan & Hughes 1998).

This paper is organized as follows. In § 2, we summarize the relevant characteristics of interferometric GW detectors. In § 3, we review the PE waveforms that we adopt. In § 4, we describe the population models that are necessary to estimate the scalings of parameters and the overall PE event rates. In § 5, we derive the expected number of PE event rates, calculate their maximum distance of detection, and estimate the implied rates of successful detections. Finally, in § 6 we summarize our conclusions and in § 7 discuss the limitations and the implications of this work.

2. OVERVIEW OF GRAVITATIONAL-WAVE DETECTORS

The new generation of GW detectors rely on interferometric monitoring of the relative (differential) separation of mirrors, which play the role of test masses, responding to space-time
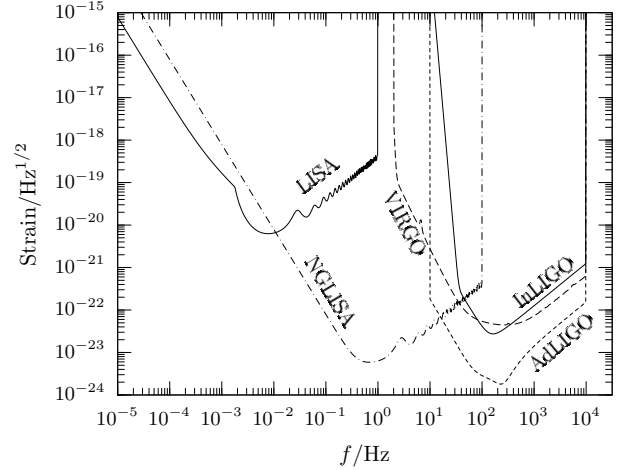

FIG. 1.— Goal sensitivity curves for interferometric GW detector facilities: InLIGO, VIRGO, AdLIGO, *LISA*, and *NGLISA*.

distortions induced by the GWs as they traverse the detectors. The effect of a GW is to produce a strain in space, which displaces the mirrors at the ends of the arms by an amount proportional to the effective arm length and GW strain. For GWs incident normal to the plane of the detector, and polarized along the arms of the detector, the mirrors at the ends of the two arms experience differential motion. Waves incident from other directions and/or polarizations also induce differential motion, albeit at a smaller level.

Presently, there is an operational international network of first generation interferometric GW detectors: InLIGO, VIRGO, TAMA, and GEO (see § 1 for references). The design of advanced terrestrial GW detector AdLIGO and space detector *LISA* is well on the way. There are also plans for a new generation of low-frequency underground detectors especially sensitive for lower frequencies (DeSalvo 2004), which might be especially sensitive to PEs, which we will discuss in a separate paper in detail. Finally, there are plans for possible future improvements of space detectors: *Decihertz Interferometric Gravitational-wave Observatory (DECIGO)* (Seto, Kawamura, & Nakamura 2001), *Advanced Laser Interferometer Antenna (ALIA)* and the *Big Bang Observer (BBO)* (Crowder & Cornish 2005). Their sensitivities, detection frequency bands and capabilities are quite different. For our purposes, a good approximation is to use: (1.) the InLIGO and VIRGO sensitivity goal (nearly reached) to assess present capabilities; (2.) the AdLIGO sensitivity goal to assess future capabilities of ground based detectors; (3.) the *LISA* sensitivity goal to assess future capabilities of initial space based detectors; and (4.) the *Next Generation LISA* sensitivity goal to assess the capabilities of possible further extensions to space detectors.

The goal RMS noise density per frequency interval for the various detectors, including instrumental and confusion noise, is plotted on Figure 1. For LIGO we adopt Abbott et. al. (2004); Lazzarini & Weiss (1996), for VIRGO we adopt Acernese et al. (2005) but for simplicity discard the narrow features[1], for AdLIGO we adopt the noise estimates from its website[2], and for *LISA*, we utilize the online sensitivity curve

[1] http : //www.virgo.infn.it/senscurve/
[2] http : //www.ligo.caltech.edu/advLIGO/scripts/ref_des.shtml

generator [3] for the instrumental noise, and adopt the confusion noise estimate from Barack & Cutler (2004a). The noise levels of possible extensions to *LISA* named the "Next Generation *LISA*" (*NGLISA*) are also provided by the sensitivity curve generator, which we also include in all of our calculations. This is very similar to the planned sensitivity curve of *DECIGO* (Seto, Kawamura, & Nakamura 2001, see the more conservative case therein) and is just halfway between *ALIA* and *BBO* (Crowder & Cornish 2005, a factor of 3 difference in sensitivity from both).

3. PARABOLIC ENCOUNTER WAVEFORMS

The GW signal waveform for PE is available in a wide range of approximations (see § 1). We adopt Turner (1977) for the angular averaged waveforms, for which the interacting masses travel on classical Newtonian trajectories and emit quadrupole radiation. Other features such as spin-spin, spin-orbit interactions, and gravitational recoil, etc., are higher order perturbations which carry only a small total signal power in typical cases. Therefore for the sake of calculating the signal-to-noise ratio, it is a sufficient first-order approximation to use these waveforms.

Illustrative examples of PE waveforms can be found in Turner (1977) (see Fig. 4 and 7 therein). The waveforms are generally constituted of a large amplitude single peak or a jump in the time domain with characteristic time scale t_0, related to the relative angular velocity at the minimum separation $\omega_0 = v_0/b_0 = 1/t_0$. Here v_0 is the relative velocity at the closest point, and b_0 is the corresponding minimum separation. Turner (1977) provides a closed analytical formula for the total GW radiation energy spectrum dE/df. The spectrum is wide-band, for parabolic orbits it is zero at $f = 0$, it has a maximum near $f_0 = \omega_0/2\pi$ and a half-width $\sim 1.5 f_0$.

The characteristic signal amplitude is obtained from the GW energy spectrum as (Thorne 1987; Flanagan & Hughes 1998)

$$h(f) = \frac{\sqrt{3}}{2\pi} \frac{G^{1/2}}{c^{3/2}} \frac{1+z}{d_L(z)} \frac{1}{f} \sqrt{\frac{dE}{df}[(1+z)f]}, \qquad (1)$$

where z is the redshift, $d_L(z)$ is the luminosity distance (Eisenstein 1997), and $dE/df\,[(1+z)f]$ is the total GW emitted energy of the source at the emitted frequency. The orientation averaged signal-to-noise ratio is

$$\left\langle \frac{S}{N} \right\rangle = \sqrt{\frac{4}{5} \int_0^\infty \frac{|h(f)|^2}{S_n(f)^2} \, df} \qquad (2)$$

where $h(f)$ is the characteristic signal amplitude (1) and $S_n(f)$ is the one-sided spectral noise density (see § 2 for references for the particular detectors). Note that the relation (2) refers to an angle-averaged SNR obtained from the cube-root of an average of cubed signal amplitudes over different possible orientations of the source and interferometer. Since event rates roughly scale with volume, i.e. distance cubed or $(S/N)^{-3}$, this prescription is useful for estimating event rates (Thorne 1987). For signals with optimal orientations, the coefficient $4/5$ in (2) is changed to 4. Note furthermore, that the $4/5$ factor is applicable for the detection rate using a single interferometric GW detector. There are already 4 interferometric GW detectors on Earth (see § 2), and it is possible that there will be a lot more in the future. A coincident analysis with multiple detectors can be used to improve the efficiency by increasing

the total signal-to-noise ratio and also by insuring that at least one detector is close to the optimal orientation (Jaronowski et al. 1996). For this reason, the coefficient $4/5$ in (2) is most likely pessimistic. For 1 detector in the optimal orientation and $K-1$ identical detectors in random orientations a quick scaling of the coefficient is $\sim 4 + (4/5)(K-1)^{1/2}$. On the other hand, a relatively large SNR might be required to keep the false alarm rate at a sufficiently low level. For a conservative estimate on the PE rate we do not modify the $4/5$ factor in the definition of SNR (2) and evaluate results for SNR = 5.

The PE waveforms can be obtained from eq. (1) by substituting the $E(f)$ relationship specific for PEs using Turner (1977):

$$h(f, f_0) = \frac{\sqrt{85}}{2^{5/3}} \pi^{2/3} \frac{G^{5/3}}{c^4} \frac{\mathcal{M}_z^{5/3}}{d_L} \frac{f_{0z}^{2/3}}{f} \sqrt{F(f/f_{0z})} \qquad (3)$$

where $\mathcal{M}_z = (1+z)(m_1 m_2)^{3/5}/(m_1+m_2)^{1/5}$ is the redshifted chirp mass if m_1 and m_2 are the masses of the interacting objects, $f_{0z} = f_0/(1+z)$ is the redshifted characteristic frequency, f denotes the observed GW frequency, and $F(x)$ is the Turner (1977) normalized dimensionless energy spectrum for dimensionless frequency $x = f/f_{0z}$, for which $\int_0^\infty F(x)\,dx = 1$.

Equation (3) is the leading order (i.e. Newtonian) approximation to the GW waveform, $h(f, f_0)$. A remarkably advantageous feature of the waveform in this approximation is that it depends on only a single combination of the orbital parameters, f_{0z}. Although we need only utilize this form (3), we briefly note that it is also possible to express the waveform with the separation at closest point b_0 in the center of mass frame (Turner 1977):

$$h(f, b_0) = \frac{\sqrt{85}}{4} \frac{G^2}{c^4} \frac{(1+z)m_1 m_2}{d_L\, b_0} \frac{1}{f} \sqrt{F[f/f_{0z}(b_0)]}. \qquad (4)$$

Here $f_{0z}(b_0)$ is the redshifted characteristic frequency for fixed initial velocity as a function of b_0. The GW amplitude spectrum $h(f, b_0)$ is roughly flat at low frequencies $f < f_{0z}$, and decreases for higher frequencies. Equation (4) shows that $h(f, b_0)$ scales with b_0^{-1} for frequencies larger than the cutoff at $\sim f_{0z}$.

Modifications are necessary for relativistic encounters. The relativistic gravitational radiation waveforms and energy output has been calculated by Martel (2004) in the quadrupole approximation for a test particle approaching a Schwarzschild black hole from infinity on a quasi-parabolic geodesic[4]. In case the periastron distance b_0 is close to the unstable circular orbit, the GW energy is significantly increased (it has a logarithmic singularity at $\lambda = 2$, where $\lambda \equiv b_0/R_{SH}$ and R_{SH} is the total Schwarzschild radius, and a factor of ~ 10 increase for $\lambda = 2.01$ or a factor of 2 for $\lambda = 3$). We adopt the fitting formula of Gair, Kennefick, & Larson (2005), which is correct within 0.1% for orbits that avoid a collision, and scale the amplitudes of the Turner (1977) waveforms (3) according to the increase of the GW energy, $E_{rel}(\lambda)/E_{nr}(\lambda)$.

$$h(f, f_0) = \frac{\sqrt{85}}{2^{5/3}} \pi^{2/3} \frac{G^{5/3}}{c^4} \frac{\mathcal{M}_z^{5/3}}{d_L} \frac{f_{0z}^{2/3}}{f} \sqrt{F\left(\frac{f}{f_{0z}}\right)} \sqrt{\frac{E_{rel}(\lambda)}{E_{nr}(\lambda)}} \qquad (5)$$

Note once again, that the dimensionless periastron distance, λ, is uniquely specified by the characteristic frequency, f_0. We

---

[4] We continue to denote as "quasi-parabolic" or simply "parabolic" encounters that have asymptotically zero velocity at infinity. Note that the trajectories are generally quite different from parabolas in the highly relativistic regime (for illustration, see Martel 2004).

derive explicit formulae for $f_0(\lambda)$ in the non-relativistic Newtonian and relativistic geodesic approximations, when considering the dynamics of PEs in § 5.1 and § 5.2 below. Quite remarkably, the characteristic frequency of the waveform is unchanged for relativistic orbits. Therefore, we do not explore the effects of relativistic modifications in the shape of the GW signal waveform, we restrict only to correcting the amplitude.

4. POPULATION MODELS

The major contribution to the PE event rate is expected from dense star clusters with a large CO fraction. The most important systems carrying these properties are possibly GCs and galactic nuclei. In this paper we focus on GCs, but simple analytical scaling of the results allows a straightforward extension to galactic nuclei or any other population of spherical star systems.

The spatial distribution of GCs exactly traces the distribution of galactic halos (Chandar, Whitmore, & Lee 2004) in the local universe. In this section we summarize the galaxy distribution and the GC abundance per galaxy, and describe the GC models which we adopt for the paper.

4.1. *Galaxy Distribution*

We utilize the local distribution of galaxies (Tully 1988). The accumulated number of galaxies to distance D can be well approximated by

$$N^{\text{gal}}(D) = \begin{cases} N_1 \, (D/\text{Mpc})^{0.9} & \text{for } D \le 3\,\text{Mpc} \\ N_2 \, (D/3\,\text{Mpc})^{1.5} & \text{for } 3\,\text{Mpc} < D < 16\,\text{Mpc} \\ N_3 \, (D/16\,\text{Mpc})^{2.4} & \text{for } 16\,\text{Mpc} < D < 60\,\text{Mpc} \\ N_4 \, (D/60\,\text{Mpc})^3 & \text{for } D > 60\,\text{Mpc} \end{cases}$$
(6)

where N_1, N_2, N_3, and N_4 are 23, 62, 1100, and 26000, respectively. The average density of faraway galaxies is $0.03\,\text{Mpc}^{-3}$, but the local galaxy abundance is much denser than average. In Eq. (6) $N^{\text{gal}}(D)$ has a 45% jump at the Virgo cluster at $D = 16\,\text{Mpc}$.

4.2. *Globular Cluster Abundance*

Following Portegies Zwart & McMillan (2000), we adopt $\bar{n}^{\text{gc}} = 2.9\,\text{Mpc}^{-3}$ for the average GC abundance in the universe. We roughly account for the clustering of GCs in the local universe by assuming that the distribution of GCs follow the abundance of galaxies. This assumption is consistent with observations (Goudfrooij et al. 2003; Chandar, Whitmore, & Lee 2004) suggesting that the population of GCs represent a universal, old halo population that is present around all galaxies. The number of GCs within a distance D is then

$$N^{\text{gc}}(D) = y^{\text{gc}} N^{\text{gal}}(D),$$
(7)

where y^{gc} is a scaling constant relating the abundance of GCs and galaxies. Using the large scale average $\bar{n}^{\text{gc}} = 2.9\,\text{Mpc}^{-3}$ (Portegies Zwart & McMillan 2000) and $\bar{n}^{\text{gal}} = 0.029\,\text{Mpc}^{-3}$ eq. (6) for $D > 60\,\text{Mpc}$ we get $y^{\text{gc}} = 100$. Alternatively, y^{gc} can be interpreted as the number of GCs per galaxy averaged over all morphological types. Concerning PE detection rates, we shall show in § 5.3 that typical observation distances for terrestrial detectors are larger than the clustering scale (6). Therefore, the results are sensitive to mainly the average abundance and are only slightly increased by the local clustering of GCs.

The value $\bar{n}^{\text{gc}} = 2.9\,\text{Mpc}^{-3}$ for the average abundance is a conservative assumption. In their quick estimate Portegies

Zwart & McMillan (2000) derived this value by adding up the contribution of galaxies of morphological types Sab, E-S0, and blue ellipticals. Recently, 12 nearby edge on spiral galaxies were examined, resulting in much larger numbers, reaching $\sim 1000 - 1300$ GCs for these particular galaxies (Goudfrooij et al. 2003; Chandar, Whitmore, & Lee 2004). In addition to the morphological types considered in Portegies Zwart & McMillan (2000), dwarf elliptical (dE) galaxies also contribute to the overall GC numbers (van den Bergh 2005). The GC content of 69 dwarf elliptical (dE) galaxies have been estimated to host about a dozen GCs per dE galaxy (Lotz, Miller, & Fergusson 2004). Therefore, our results on detection rates correspond only to lower limits, which has to be scaled linearly with $\bar{n}^{\text{gc}}$ when more detailed estimates become available.

The GC distribution given by (6–7) is only valid for subcosmological scales. Assuming that D denotes the luminosity distance, d_{L}, in eqs. (6–7) which is a direct observable using the GW amplitude, the change in the cosmological volume element decreases the average density.

$$N^{\text{gc}}(d_{\text{L}}) = 4\pi \int_0^{z(d_{\text{L}})} \frac{\partial V}{\partial z \partial \Omega} y^{\text{gc}} \bar{n}^{\text{gal}} \, dz$$
(8)

We adopt the cosmological volume element (Eisenstein 1997) for a ΛCDM cosmology with $(\Omega_m, \Omega_\Lambda, h) = (0.3, 0.7, 0.7)$ consistent with recent observations of the *Wilkinson Microwave Anisotropy Probe* and the Sloan Digital Sky Survey (Tegmark et al. 2004). We find that the uncorrected volume element $d_{\text{L}}^2 d\Omega dd_{\text{L}}$ is reduced by a factor of 0.7 for $z = 0.1$ ($d_{\text{L}} = 0.5\,\text{Gpc}$) and by a factor of 0.053 for $z = 1$ ($d_{\text{L}} = 7\,\text{Gpc}$). Since GCs are believed to represent an old halo population in galaxies, we do not account for additional possible cosmological evolution of the comoving GC abundance.

4.3. *Globular Cluster Models*

Here we define the GC models that we use to obtain typical PE parameters and event rates. First we define the common features that are the same for both of our models. We assume a total of N^{tot} stellar mass stars, $m_{\text{star}} = M_\odot$, spherically distributed within a typical radius R_{gc}. Also within the cluster, is a CO population consisting of $N_{\text{CO}} \equiv q N^{\text{tot}}$ objects with $q \ll 1$ that move in the background gravitational potential of the stars. We define the "typical CO mass" as $\langle m_{\text{CO}} \rangle = 10 M_\odot$. We adopt typical values of $N^{\text{tot}} = 10^6$, $R_{\text{gc}} = 1\,\text{pc}$, $N_{\text{CO}} = 10^3$, with $q = 10^{-3}$, and $\langle m \rangle \simeq M_\odot$ (Djorgovski & Meylan 1994; Portegies Zwart & McMillan 2000; Miller 2002).

We construct two different models for the distribution of mass, spatial coordinate, and velocities of stars. Model I is a simple plausible model to get the scaling of PE event rates on different cluster parameters. Here we assume a homogeneous spherical distribution, and the COs within the cluster have the same mass and magnitudes of velocities. In Model II, we refine the assumptions to account for the distributions of masses, mass segregation, and relative velocity distributions.

By comparing Models I and II, we find that while Model I gives the correct R_{gc}, N^{tot}, N_{CO}, and f_0 scalings, it underestimates the total event rate of a single GC by 2 orders of magnitudes. The comparison of Models I and II is necessary (i) to understand the origin of the large increase in PE event rates as compared to Dymnikova, Popov, & Zentsova (1982), and (ii) to understand the impact on the BH mass function of GCs on PE event rates. It is therefore emphasized that the GC model assumptions have a crucial importance when determining the

PE event rate. We believe that our Model II includes all of the essential features of GCs for the assessment of PE rates, and uncertainties are comprised of the uncertainties in the model parameters rather than additional fundamental processes[5].

4.3.1. *Model I*

For the most simple model, the spatial distribution is assumed to be uniform within a characteristic radius $R_{\rm gc}$, and it is assumed that all COs have the same mass $m_{\rm CO} = 10 {\rm M}_\odot$ and magnitude of velocity $v_{\rm vir}$. The orientation of velocities is isotropic, implying a velocity dispersion of $\sigma \simeq v_{\rm vir}$. For this simple model, we estimate the relative velocity distribution of COs to be the same as the individual velocities $v_{\rm rel} \simeq v_{\rm vir}$. The characteristic velocities can be obtained from the virial theorem for a uniform distribution of mass[6]:

$$v_{\rm vir} = \sqrt{\frac{3}{5} \frac{G N^{\rm tot} \langle m \rangle}{R_{\rm gc}}} \qquad (9)$$

The PE event rate is calculated as the rate of scattering on a fixed target lattice, with incident velocity $v_{\rm vir}$.

4.3.2. *Model II*

We improve Model I with the following factors. The validity and motivation of these assumptions is discussed below the list.

1. We assume an equal number of NSs and BHs $N_{\rm NS} = N_{\rm BH}$. We introduce $g_{\rm BH}(m) = 0.5[\ln(m_{\rm max}/m_{\rm min})]^{-1} m^{-1}$ for the fractional distribution of BH masses among COs with mass m per mass interval dm, in the range $m_{\rm min} < m < m_{\rm max}$, with $\int g_{\rm BH}(m) dm = 0.5$. We define the NS mass distribution $g_{\rm NS}(m)$ as a Gaussian distribution with norm 0.5, mean $1.35 {\rm M}_\odot$, and variance $0.1 {\rm M}_\odot$. Finally we define the CO distribution by $g_{\rm CO}(m) = g_{\rm BH}(m) + g_{\rm NS}(m)$, which has a unit norm. For definiteness, we take $N_{\rm BH} = 500$, $m_{\rm min} = 5 {\rm M}_\odot$, and $m_{\rm max} = 60 {\rm M}_\odot$, implying that $\langle m_{\rm BH} \rangle \simeq 20 {\rm M}_\odot$ and $\langle m_{\rm CO} \rangle \simeq 10 {\rm M}_\odot$, but also calculate detection rates for more general BH mass distributions. The PE detection rates are practically independent of the actual total number and distribution of NSs.

2. We account for the mass segregation by assuming thermal equipartition among COs, objects with mass m have a velocity $v_m = (m/\langle m \rangle)^{-1/2} v_{\rm vir}$, and are confined within a radius, $R_m = (m/\langle m \rangle)^{-1/2} R_{\rm gc}$, while regular stars are distributed uniformly within a sphere of radius $R_{\rm gc}$, as in Model I. Since $N \gg N_{\rm CO}$, the background gravitational potential is determined by regular stars. See Fig. 2 for an illustration. For core collapsed models a modified scaling is necessary (see text below).

3. The relative velocity for COs with masses m_1 and m_2 is assumed to be $v_{\rm rel} \equiv v_{12} = [(m_1^{-1} + m_2^{-1}) \langle m \rangle]^{1/2} v_{\rm vir}$.

The BH mass distribution is crucial for the analysis, since signal rates scale with $m^{19/3}$ (see § 5 and the appendix below).
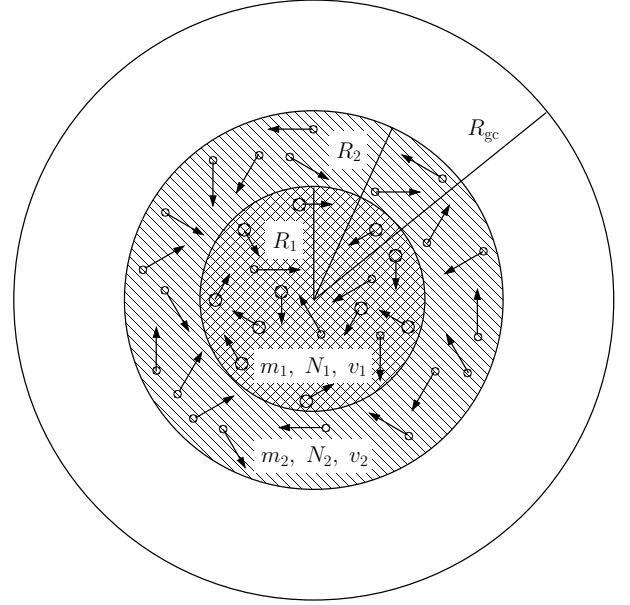

FIG. 2.— Encounters for Model II. More massive COs $m_1 > m_2$ are distributed uniformly within a sphere of smaller radius $R_1 < R_2$ and have smaller velocities. PEs between COs with m_1 and m_2 can take place within R_1. The relative velocity before the interaction is $v_\infty = v_{12}(m_1, m_2)$. Note that Model II assumes a continuous mass function, for which N_1 and N_2 are in fact infinitesimal.

Unfortunately, the analysis of BH mass functions have not yet converged. Recent X-ray observations display evidence for 20 galactic BHs with masses between $4 \lesssim m/{\rm M}_\odot \lesssim 14$ (Casares 2005), and ~ 45 ultra-luminous X-ray sources are identified with intermediate-mass black holes (IMBHs) with masses $m = 10^2 - 10^4 {\rm M}_\odot$ (Ptak & Colbert 2004; Miller & Colbert 2004; Gebhardt, Rich, & Ho 2005; Blecha et al. 2005). Theoretical predictions from two-dimensional simulations of stellar core collapse (Fryer & Kalogera 2001) lead to masses smaller than $20 {\rm M}_\odot$ with very different distributions depending on the assumptions (fraction of explosion energy used to unbind the star, stellar winds, mass transfer after helium ignition). Sophisticated simulations of the initial phase of rapid star evolution assuming a lower metallicity for the progenitor stars (weaker stellar winds) appropriate for GCs and including a large fraction of binaries, collisions, and accretion leading to the mass buildup of BHs imply an initial smooth decreasing distribution of stellar-mass BHs with masses up to $\sim 60 - 100 {\rm M}_\odot$ (Belczynski et al. 2005) depending on model assumptions and cluster environments. Results are valid for timescales short compared to later dynamical evolution of the cluster. However, the final fate of the cluster remains highly uncertain. In small GCs, dynamical interactions of binaries might eject a significant portion of the stellar-mass BH population (Sigurdsson & Hernquist 1993; Portegies Zwart & McMillan 2000; O'Leary et al. 2006). Following Miller (2002) and Will (2004) we adopt $g_{\rm BH}(m) \propto m^{-1}$ leaving the minimum and maximum masses free parameters. However, most recent population synthesis simulations (Belczynski et al. 2005) typically yield steeper BH mass functions. For this reason we felt it important to compute results for other distributions $g_{\rm BH}(m) \propto m^{-p}$ with $p = 0$, 1, and 2, as well. Concerning the other parameters, in our standard model we take $m_{\rm min} = 5 {\rm M}_\odot$ and $m_{\rm max} = 60 {\rm M}_\odot$, for which $\langle m_{\rm BH} \rangle \simeq 20 {\rm M}_\odot$ and $\langle m_{\rm CO} \rangle \simeq 10 {\rm M}_\odot$, and assume $N_{\rm BH} = 500$, but also calculate re-

---

[5] For example, details like bound binary populations and interactions are not essential for PEs, and Spitzer instability and core collapse can be accounted for by choosing our model parameters accordingly (see § 7.3.3 for a discussion).

[6] There is a similar result for a spherical star system of polytropic distribution with a root mean square radius R. The only difference is in the 3/5 factor of Eq. 9, which becomes 1/2 in that case (e.g. Saslaw 1985).

sults for other N_{BH}, m_{min}, and m_{max} values.

The NS mass distribution that we utilize is supported by observations of 26 radio pulsars and 4 X-ray binaries (Postnov & Prokhorov 2003, and references therein). The distribution is sharply peaked around $1.35 M_\odot$. Our assumption on the total number of NSs ($N_{NS} = 500$) is somewhat arbitrary, values could be higher or lower depending on what fraction of NSs are ejected by kicks during their formation. Our detection rate estimates can be scaled to the appropriate value using $\nu_{NS-NS} \propto N_{NS}^2$ and $\nu_{BH-NS} \propto N_{NS}N_{BH}$ (see § 5 below). Note however, that in § 5 we show that NS interactions contribute a negligible fraction of the PE event rate (see Figs. 6 and 7 below).

Note that we do not consider encounters between white dwarfs (WDs). The detection of PEs between WDs are even worse than for NSs, since WD masses are even smaller (Binney & Tremaine 1987). Our final results show that the PE detection rates roughly scale with $\sim m^{8.33}$, implying that rates are enormously suppressed for WDs: by a factor of $\sim 10^{15}$ relative to $50 M_\odot$ BHs, which are typical for detection (see Fig. 6). Moreover, WDs are disrupted by tidal torques for close encounters, at sub-Hz frequencies. Therefore, PEs of WDs are completely invisible for terrestrial detectors.

The second improvement is to account for mass segregation. The differentiation of the stellar population with mass within the cluster core is a consequence of thermal equilibrium (Binney & Tremaine 1987). Objects with masses larger than $10 M_\odot$ had enough time to relax to thermal equilibrium within the lifetime of the GCs (Farouki & Salpeter 1982). This means that the kinetic energies of each of the component stars are drawn from the same distribution, implying that the typical speed of an object of mass m is $v_m = (m/\langle m \rangle)^{-1/2} v_{vir}$, causing the object to sink to the core of the cluster. For a nearly homogeneous distribution of background stars, this implies that the maximum radius available to a given mass is $R_m = (m/\langle m \rangle)^{-1/2} R_{gc}$ (Binney & Tremaine 1987). For the BH distribution given by $g_{BH}(m)$ we get that BHs with mass $\sim 50 M_\odot$ (which make the dominant contribution to PE rates, see Figs. 6 and 7 below) are confined to a radius $\sim 0.14 R_{gc}$. Note that our scalings based on thermal equipartition might not hold in case Spitzer instability leads to core collapse, creating a dynamically decoupled core of high mass BHs (typically $R_{core} \sim 0.01$–$0.10 R_{gc}$ depending on the fraction of primordial binaries, Heggie, Trenti, & Hut 2006). We can account for core collapse by simply scaling our final results on detection rates appropriately with $N_{BH}^2 R_{core}^{-3} v_{core}^{-1}$ (see § 7.3.3 for a discussion).

Finally, we discuss the assumption on the relative velocity. The velocity distribution of stars in GCs is well described by the King-Michie (KM) model (Meylan 1987), which is roughly a Maxwell-Boltzmann (MB) distribution with a maximum velocity cutoff. It is well-known that the relative velocity distribution for MB individual velocity distributions is also MB for the reduced mass $\mu = m_1 m_2/(m_1 + m_2)$ (Binney & Tremaine 1987). Thus $\langle v_{12} \rangle_{RMS} = (m_1/\mu)^{1/2} \langle v_{m_1} \rangle_{RMS} = [(m_1^{-1} + m_2^{-1})\langle m \rangle]^{1/2} v_{vir}$.

Note that we do not utilize the exact velocity distribution, but associate the same fixed velocity value for every object with identical masses. Relaxing this approximation and accounting for MB velocity distributions leads to a change of only a few percent in the encounter rate results (the correction is $(3/\pi)^{1/2}$ for Model I in the range of GW detector frequencies, see Kocsis & Gáspár 2004 for the derivation). Thus,

the velocity distribution can be safely approximated with the mean value. A simple explanation is the fact that GW detector frequencies correspond to unbound encounters with nearly parabolic trajectories, for which the exact value of the initial velocity is negligible (see § 5.1 below).

The PE event rate for component masses m_1 and m_2 is calculated as the rate of scattering with incident velocity equal to the initial relative velocity $v_{rel} \equiv v_{12}(m_1, m_2)$.

5. PARABOLIC ENCOUNTER EVENT RATE

We now derive the event rate for the successful detection of PE signals using the two models of GCs. This section is divided in five parts. In § 5.1 we derive the comoving event rate per comoving characteristic frequency bins for individual GCs for the two population models. In § 5.2 we derive the modifications necessary for relativistic encounters. In § 5.3 we determine the signal-to-noise ratio using the specific detector sensitivity curves and determine the maximum observable distance of PEs. In § 5.4, we add up the contributions of all possible GCs within the visible distance and estimate the PE detection rates. Finally in § 5.5 we conclude the results of the analysis.

5.1. *Contributions of Individual Globular Clusters*

5.1.1. *Outline*

When calculating the detectable event rates for specific GW detectors, it is desirable to express the encounter cross section for particular f_0 frequency bins. To achieve this we first compute the interaction cross-sections for given masses and initial orbital parameters. Then, the Newtonian equations of motion relate the initial orbital parameters to f_0. Changing to the f_0 variable leads to the partial event rate for the given masses and characteristic encounter frequencies. Then, for Model I, it is very simple to add up the individual contributions of all objects within the cluster. For Model II, we utilize the specific radial and relative velocity distributions, R_m and v_{12}, and average over the CO mass distribution.

5.1.2. *Derivation of Event Rates*

The typical minimum distance between COs in these systems is $R_{gc}/\sqrt[3]{N} \simeq 10^{11}$ km, a value several orders of magnitudes larger than the typical minimum separation of an encounter (10 km $< b_0 \lesssim 10^7$ km for detectable frequencies, see Eq. [14] below). Therefore, a sufficient approximation is to consider short-time two-body interactions during encounters[7], and constant velocities in between events. The PE event rate can then be simply estimated by a scattering of particles with incident initial velocities $v_\infty = v_{rel}$ on a still target lattice.

Since the velocities are assumed to be locally isotropic everywhere in the cluster, the cross section of a particle with an impact parameter between b_∞ and $b_\infty + db_\infty$ is $d\sigma = 2\pi b_\infty db_\infty$. We proceed to express the infinitesimal cross section for df_0 bins.

We derive encounter parameters with a non-relativistic Newtonian description. The separation, b_0, and relative velocity, v_0, at periastron can be computed from the initial conditions of the interacting bodies. The initial parameters are the impact parameter b_∞ and the velocity, $v_\infty \equiv v_{rel} \equiv$

---

[7] We shall discuss below that the PE event rate is not sensitive on whether the interacting participants are elements of regular bound binaries or if they are single objects.

$v_{12}(m_1, m_2)$, of the scattered particle (see § 4.3.2 for the definition). Using the conservation of mechanical energy and angular momentum we get

$$b_\infty = \frac{b_0}{\sqrt{1-2\gamma}}, \quad \text{and} \quad v_\infty = v_0 \sqrt{1-2\gamma}, \qquad (10)$$

where $\gamma = (GM)/(b_0 v_0^2)$ is the ratio of potential energy and double kinetic energy at the closest point[8], with $M = m_1 + m_2$. Although Eq. (10) is strictly only valid in the comoving reference frame of the center-of-mass, it is an adequate approximation for the realistic parameters as long as $v_\infty \ll v_0$. Again, we point out that the relevant encounters are nearly parabolic, so that the initial velocity distributions have a negligible impact on the result.

Let us express the cross section with variables b_0 and v_∞ using Eq. (10) and make use of our simplifying assumption that v_∞ is a constant for fixed masses (see § 4.3). The result is

$$d\sigma = \left(\frac{GM}{v_\infty^2 b_0} + 1 \right) 2\pi b_0 db_0. \qquad (11)$$

Here, the first term dominates the parenthesis for typical v_∞ and b_0 values (see Eq. 14. below). This term is responsible for the deflection of trajectories due to gravity.

The characteristic GW frequency is directly related to the minimum separation, b_0, and the relative velocity v_0 at b_0 by

$$\omega_0 = 2\pi f_0 = \frac{v_0}{b_0}. \qquad (12)$$

Using Eq. (10),

$$\omega_0 = (2GM)^{1/2} b_0^{-3/2} \left(1 + \frac{v_\infty^2 b_0}{2GM} \right)^{1/2}. \qquad (13)$$

For typical frequency bands of InLIGO (*LISA*) the correction on the RHS is $v_\infty^2 b_0 / (2GM_{CO}) \lesssim 10^{-8}$ (10^{-4}) for InLIGO (*LISA*). In order to get the event rate per frequency bin, we need the inverse relationship $b_0(\omega_0, v_\infty)$. This can be obtained recursively, as a power series in ω_0. To the second non-vanishing order, we get

$$b_0 = (2GM)^{1/3} \omega_0^{-2/3} \left(1 + \frac{1}{3} \frac{v_\infty^2}{(2GM)^{2/3}} \omega_0^{-2/3} \right). \qquad (14)$$

Substituting in Eq. (11) yields

$$d\sigma = \frac{2\pi}{3} \frac{(2GM)^{4/3}}{v_\infty^2} \omega_0^{-2/3} \left(1 + \frac{8}{3} \frac{v_\infty^2}{(2GM)^{2/3}} \omega_0^{-2/3} \right) \frac{d\omega_0}{\omega_0}. \qquad (15)$$

For Model I, the scattering rate for a single particle is $n_{CO} v_\infty d\sigma$, where n_{CO} is the number density of COs. Since there are a total of N_{CO} particles, the contribution of all COs is $1/2 \times N_{CO} n_{CO} v_\infty d\sigma$, where the $1/2$ factor comes from the fact that the same ensemble of particles constitute both the targets and the injection. Thus Eq. (15) becomes

$$d\nu^I = \nu_1^I \left(\frac{f_0}{f_{100}} \right)^{-2/3} \left(1 + \left(\frac{f_0}{f_1^I} \right)^{-2/3} \right) \frac{df_0}{f_0}. \qquad (16)$$

where $f_{100} = 100$ Hz and

$$\nu_1^I = (2\pi)^{-2/3} \frac{N_{CO}^2}{4} \frac{(4GM_{CO})^{4/3}}{R_{gc}^3 v_\infty} f_{100}^{-2/3} = 6.7 \times 10^{-15} \, \text{yr}^{-1} \quad (17)$$

$$f_1^I = \frac{1}{2\pi} \left(\frac{8}{3} \right)^{3/2} \frac{v_{vir}^3}{4GM_{CO}} = 1.7 \times 10^{-8} \, \text{Hz}. \qquad (18)$$

[8] $\gamma < 1/2$ for hyperbolic Newtonian trajectories.

For Model II, the interacting objects with masses m_1 and m_2 are distributed uniformly within radii R_1 and R_2 and have mass-dependent relative velocities $v_\infty = v_{12}$ (see Fig. 2). Let N_1 and N_2 denote the number of particles with mass m_1 and m_2, respectively. Let us assume $m_1 > m_2$, for which $R_1 < R_2$. In this case the interactions between masses m_1 and m_2 take place only within a radius R_1, where the density of particles with mass m_2 is $n_2 = N_2 / (R_2^3 4\pi/3)$. For a smooth distribution, N_1 is the infinitesimal number of particles with masses between m_1 and $m_1 + dm_1$, i.e. $N_1 = N_{CO} g_{CO}(m_1) dm_1$ (and N_2 defined similarly). The scattering rate for an injection of N_1 particles with v_∞ velocities on a target density n_2 is is $N_1 n_2 v_\infty d\sigma$. To get the total event rate for the cluster for ω_0 bins we need to integrate over the mass distributions

$$d\nu^{II} = \int_0^\infty dm_1 g_{CO}(m_1) \int_0^\infty dm_2 g_{CO}(m_2) \times$$
$$\left[\nu_1^{II}(m_1, m_2) \left(\frac{f_0}{f_{100}} \right)^{-2/3} + \nu_2^{II}(m_1, m_2) \left(\frac{f_0}{f_{100}} \right)^{-4/3} \right] \frac{df_0}{f_0}, \qquad (19)$$

where $\nu_1^{II}(m_1, m_2)$ and $\nu_2^{II}(m_1, m_2)$ are given by

$$\nu_1^{II}(m_1, m_2) = (2\pi)^{-2/3} \frac{N_{CO}^2}{4} \frac{(2GM)^{4/3}}{R_>^3 v_\infty} f_{100}^{-2/3} \qquad (20)$$

$$\nu_2^{II}(m_1, m_2) = (2\pi)^{-4/3} \frac{2N_{CO}^2}{3} \frac{(2GM)^{2/3} v_\infty}{R_>^3} f_{100}^{-4/3} \qquad (21)$$

where $R_> = \max(R_1, R_2)$ and the mass dependence is implicit in the total mass M, $v_\infty = v_{12}$, R_1, and R_2 (see the Appendix for explicit formulae).

The mass integrals in (19) can be evaluated independent of the frequency, resulting in the same functional form as for Model I (16). The constants for Model II are

$$\nu_1^{II} = 1.9 \times 10^{-12} \, \text{yr}^{-1} \qquad (22)$$

$$f_1^{II} = 1.0 \times 10^{-10} \, \text{Hz}. \qquad (23)$$

(see the Appendix for parametric formulae).

For Model II, it is also interesting to get the relative encounter rates for BH−BH, BH−NS, and NS−NS interactions. Integrating Eq. (19) over the corresponding mass intervals, we get

$$\nu_{1,BH-BH}^{II} = 0.996 \, \nu_1^{II} = 286 \, \nu_1^I, \qquad (24)$$

$$\nu_{1,BH-NS}^{II} = 4.14 \times 10^{-3} \nu_1^{II} = 1.19 \, \nu_1^I, \qquad (25)$$

$$\nu_{1,NS-NS}^{II} = 7.04 \times 10^{-5} \nu_1^{II} = 0.02 \, \nu_1^I. \qquad (26)$$

The corresponding analytical formulas are given in the Appendix. It is clear that BH−BH encounters dominate the event rates. The event rates of NS−NS encounters are more than four orders of magnitude lower!

5.1.3. Discussion

Therefore we conclude that Model II has a much larger event rate than Model I. By inspection of Eq. (19) and (20) the main factors responsible for this increase can be identified. First, the CO density is increased by the CO confinement in the core: $n \propto R_m^{-3} \propto m^{3/2}$. Second, the typical CO relative velocity inverse is increased: $v_\infty^{-1} \propto m^{1/2}$. Third, the gravitational focusing is proportional to $m^{4/3}$. Thus, $\nu_1 \propto \left(R_{gc}^3 / R_{CO}^3 \right) \times \left(\langle m^{10/3} \rangle / m_{CO}^{10/3} \right)$. The PE event rate is thus

highly inclined towards the high-mass end of the BH distribution in the cluster. For a more precise treatment, the exact contributions of the component mass parameters are given in the Appendix, Eqs. (A4-A6). Note, that Dymnikova, Popov, & Zentsova (1982) obtained results equivalent to our Eq. (17) of Model I, but they focus on star – star encounters and use $m = 4M_\odot$ instead of $m_{CO} = 10M_\odot$. (Another difference is that they do not discuss f_0-dependent differential rates, but derive the total PE rate based on a typical minimum separation. Using $m = 4M_\odot$ in Model I, the results are a factor of 10^3 lower than the rates for Model II.)

Equations (16-18) and (22-23) give the resulting PE event rate per GC of all Newtonian trajectories between point masses for the two GC models considered. A significant shortcoming is that COs have finite radii and collide for sufficiently small minimum separations. Moreover the Newtonian approximation breaks down for large velocities or strong gravitational fields. These effects are considered in § 5.2 below.

Notice how small is the correction proportional to $f_0^{-4/3}$ in Eq. (16) for GW detector frequencies $f \gg f_1^{I,II}$. Recall that in Eqs. (13) and (14) the expansion coefficient is proportional to v_∞. Hence the leading order term is exact for $v_\infty = 0$, thus it corresponds to parabolic trajectories. This proves our conjecture that the unbound orbit encounter rate is dominated by near-PEs.

In Eq. (16) the leading-order terms are proportional to $1/v_{vir}$. The result is slightly counterintuitive if one identifies the star system with an ideal gas, since for ideal gases, the rate of collisions is directly proportional to v_∞. In this perspective it seems reasonable to expect the encounter rate to be a growing function of v_∞ for fixed frequency bins. The confusion arises from the fact that our GC models are using the opposite limit. For star systems the typical velocities are so small that the gravitational interaction dominates the motion of the stars.[9] Increasing the velocities decreases the gravitational focusing, thereby decreasing the encounter likelihood.

The expected rate of PE events for a single GC is plotted in Figure 3 for logarithmic frequency bins for the two GC models. The non-relativistic results presented in this section are plotted with dotted lines, which overlap with the relativistic calculation below ~ 10 Hz. For higher frequency the minimum separation drops below ~ 6 Schwarzschild radii for the largest BHs and relativistic corrections become important. Figure 3 displays that event rates are higher for lower characteristic frequencies, e.g. for model II for $f_0 = 0.1$ mHz (the minimum frequency for space detectors), we get 1.9×10^{-8} yr^{-1}GC^{-1} events, whereas for terrestrial detectors $f_0 = 100$ Hz it is only 1.9×10^{-12} yr^{-1}GC^{-1}.

5.2. Relativistic Orbits

Up to this point the PE event rates have been estimated for fixed characteristic frequencies but independent of the minimum separation b_0 and relative velocity v_0. In addition to non-relativistic parabolic encounters, these events also include head-on collisions, relativistic captures, relativistic flybys, and zoom-whirl orbits. Since we have used a Newtonian analysis in the derivation, our results presented in § 5.1

---

[9] The ideal gas model is sufficient only for extremely small characteristic frequencies $f_0 \ll f_1$ (eqs. [18] and [23]), which is below the lower frequency limit of GW detectors. In this regime the stars' trajectories are only slightly deflected, implying that gravity, in terms of encounter likelihood, is negligible.
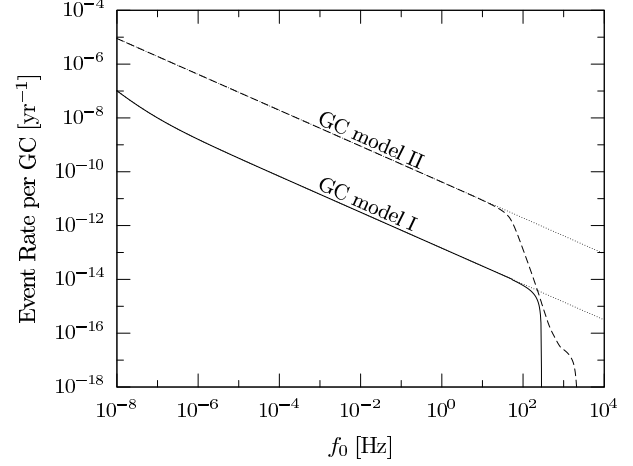

FIG. 3.— The expected total rate of PEs produced in a single GC per logarithmic frequency bin. GC Model I (solid) and Model II (dashed) results are shown including relativistic corrections for geodesics avoiding head-on collisions (see § 5.2). The dotted lines represent PE event rates in the non-relativistic approximation. The non-relativistic treatment is adequate for low frequencies for which the trajectories avoid collisions with minimum separations of several Schwarzschild radii. Only a fraction of these events can be detected, depending on the distance of the GC.

are valid for the non-relativistic parabolic encounters only. Here, we improve the classical calculation to account for general relativistic encounters of test particles moving along geodesics in the Schwarzschild space-time. This treatment is exact for extreme mass ratios, but as an approximation we extrapolate these formulas for general mass-ratios as well.

To classify the orbits, we introduce a parameter $\lambda \equiv b_0/R_{SH}$, where b_0 is the distance at periastron, and $R_{SH} = 2GM/c^2$ is the Schwarzschild radius of the total mass[10]. For Newtonian parabolic encounters, we get $\lambda = c^2/v_0^2$. We distinguish (i) non-relativistic parabolic encounters for $\lambda \geq 6$, (ii) general relativistic flybys for $2.1 < \lambda < 6$, (iii) zoom-whirl orbits for $2 \leq \lambda \leq 2.1$, and (iv) head-on collisions for $2 < \lambda$. We restrict our calculations to $\lambda \geq 2$, since this is the regime in which matched filtering can be carried out using the waveforms of § 3.

In this section, we improve § 5.1.2 to account for the relativistic deviations in the trajectories. In practice, we repeat the derivation of § 5.1.2 to get the cross-section using the orbital parameters of the geodesics of a test particle moving in a Schwarzschild space-time (Gair, Kennefick, & Larson 2005).

For parabolic encounters the specific orbital angular momentum is

$$\widetilde{L} = \sqrt{2GMb_0} \left(1 - \lambda^{-1}\right)^{-1/2}, \qquad (27)$$

where $\lambda = \lambda(b_0)$ defined above. The non-relativistic result is retained for $\lambda \to \infty$. Equating (27) to the angular momentum before the encounter $\widetilde{L} = b_\infty v_\infty$, solving for b_∞, and substituting in $d\sigma = 2\pi b_\infty db_\infty$ we get

$$d\sigma = \frac{GM}{v_\infty^2 b_0^2} \frac{1 - 2\lambda^{-1}}{(1 - \lambda^{-1})^2} 2\pi b_0 db_0. \qquad (28)$$

This is to be compared to the non-relativistic analogue (11). The first term is the non-relativistic term for near-parabolic orbits and the λ-dependent fraction describes the relativistic

---

[10] Here we restrict to BH-BH encounters which dominate event rates, see Eqs. (24-26).

correction. The latter decreases the cross section per unit b_0. For $\lambda \to 2$ the cross section becomes 0. For smaller impact parameters a head-on collision takes place, for which the periastron distance and λ is undefined.

Repeating § 5.1.2, the next step is to change to the f_0 characteristic frequency variable. Since $\widetilde{L} = b_0^2 \, d\phi/d\tau$, where $d\tau = (1-\lambda^{-1})^{1/2} \, dt$ is the infinitesimal proper time element along the geodesic at the closest approach (e.g. Misner, Thorne, & Wheeler 1973), from (27) we get

$$\frac{d\phi}{dt} \equiv \omega_0 \equiv 2\pi f_0 = (2GM)^{1/2} b_0^{-3/2}. \qquad (29)$$

Quite remarkably, this is identical to the result of the non-relativistic calculation for parabolic orbits (13). The GW waveforms have a peak at an angular frequency ω_0 for the non-relativistic encounters (Turner 1977, and see § 3 above). For relativistic zoom-whirl orbits with several revolutions around the central BH, the most intensive GWs are radiated at twice the orbital frequency. It is also useful to get the inverse relationship from eq. (29):

$$\lambda(M, f_0) = \left(\frac{c^3}{4\pi G} \frac{1}{M f_0} \right)^{2/3}. \qquad (30)$$

According to Eq. (29), the non-relativistic result for ω_0 is adequate even in this regime. Using (13) we get

$$d\sigma = \frac{2\pi}{3} \frac{(2GM)^{4/3}}{v_\infty^2} \omega_0^{-2/3} \frac{1-(\omega_0/\omega_{M,\max})^{2/3}}{\left[1-\frac{1}{2}(\omega_0/\omega_{M,\max})^{2/3}\right]^2} \frac{d\omega_0}{\omega_0}, \quad (31)$$

analogous to (15) for parabolic orbits, where

$$\omega_{M,\max} \equiv 2\pi f_{M,\max} \equiv \frac{2\pi c^3}{\sqrt{32} GM} \qquad (32)$$

is the maximum angular frequency, corresponding to $\lambda = 2$.

It is desirable to calculate the partial event rates of PEs with minimum separations b_0 exceeding λR_{SH}, we substitute in Eq. (13), and impose the resulting constraint on the characteristic frequency:

$$f_0 \leq f_{M,\lambda} = 2\pi \frac{c^3}{2GM} \lambda^{-3/2}. \qquad (33)$$

For marginally plunging orbits, $\lambda = 2$, we get $f_{M,\lambda} = f_{M,\max}$.

When adding up the total event rates for a particular f_0 (Eqs. 16 and 19) only the masses satisfying the constraint (33) have to be included in the mass integrals. Repeating § 5.1.2 with these modification, we get for Model I

$$d\nu^I = \nu_1^I \left(\frac{f_0}{f_{100}} \right)^{-2/3} \frac{1-2(f_0/f_{M,\max})^{2/3}}{\left[1-(f_0/f_{M,\max})^{2/3}\right]^2} \frac{df_0}{f_0}. \qquad (34)$$

for $f_0 \leq f_{M_{CO},\lambda}$, and $d\nu^I = 0$ otherwise. For Model II, we get

$$d\nu^{II} = \iint_{f_0 \leq f_{M,\lambda}} dm_1 dm_2 \, g_{CO}(m_1) g_{CO}(m_2) \times$$
$$\nu_1^{II}(m_1, m_2) \frac{1-2(f_0/f_{M,\max})^{2/3}}{\left[1-(f_0/f_{M,\max})^{2/3}\right]^2} \left(\frac{f_0}{f_{100}} \right)^{-2/3} \frac{df_0}{f_0}, \qquad (35)$$

In Eqs. (34) and (35) ν_1^I and $\nu_1^{II}(m_1, m_2)$ are the non-relativistic terms given by (17) and (20).

Fig. 3 shows the resulting total event rates for $d\ln f_0$ intervals. The solid and dashed lines represent the total event rates of PEs for Models I and II, respectively, including the relativistic correction for encounters that avoid collisions. As a comparison, dotted lines display non-relativistic results. Compared to the non-relativistic results, event rates decrease for two reasons: first the gravitational focusing decreases the cross sections of relativistic orbits, for $2100\,\mathrm{Hz} = f_{0,\max}[2m_{NS}, (\lambda=2)] \gtrsim f_0 \gtrsim f_{0,\max}[2m_{\max}, (\lambda=6)] = 10\,\mathrm{Hz}$, and second, the plunging orbits with $\lambda < 2$ are excluded from our estimate. The latter effect kicks in at $f_{0,\max}(2m_{\max}, 2) > 47\,\mathrm{Hz}$ where the highest mass BHs suffer head-on collisions. At $f_{0,\max}(2m_{\min}, 2) = 570\,\mathrm{Hz}$ even the smallest BHs are captured, and only the NS–NS PE event rate contributions remain. The NS–NS partial event rates can be visualized for lower frequencies by extrapolating the total event rates shown in Fig. 3 between $570\,\mathrm{Hz} < f_0 < 2100\,\mathrm{Hz}$. The NS–NS event rates are clearly negligible compared to the total rates including BHs. Note, that our calculations use point masses valid for BHs only. For $f_0 \gtrsim 1500\,\mathrm{Hz}$ the minimum separation of $1.35 M_\odot$ NSs decreases under $\sim 20\,\mathrm{km}$, for which our approximation breaks down.

Figure 3 is useful to visualize the total PE event rate per GC. However, only a fraction of these events can be detected, and this fraction depends on both the differential encounter event rates $\partial^3\nu/\partial m_1 \partial m_2 \partial \ln f_0$ and also the observable distance of the encounter. For the detection rates we shall make use of the infinitesimal encounter event rate for infinitesimal mass and f_0 bins. From eq. (35) we get[11]

$$\frac{\partial^3\nu}{\partial m_1 \partial m_2 \partial \ln f_0} = \nu_1^{II}(m_1, m_2) \frac{1-2(f_0/f_{M,\max})^{2/3}}{\left[1-(f_0/f_{M,\max})^{2/3}\right]^2} \left(\frac{f_0}{f_{100}} \right)^{-2/3}. \qquad (36)$$

The *total event rate* for one GC depends only on $\partial^3\nu/\partial m_1 \partial m_2 \partial \ln f_0$, thus in eq. (35) eq. (36) was directly integrated over f_0, and the m_1, and m_2 distributions. However for the *detection rate*, the observation distance of the encounter depends on f_0, m_1, and m_2 differently. Therefore the differential *detection rate* has a modified parameter dependence, implying that the integration can be carried out only after the observation distance had been included in the differential rate.

5.3. *Maximum Distance of Detection*

We now derive the maximum detectable distance of an encounter for fixed masses m_1, m_2, and characteristic frequency f_0, for a given signal-to-noise ratio S/N. The luminosity distance can be expressed with the redshifted parameters, $m_{iz} = (1+z)m_i$ for $i = \{1, 2\}$ and $f_{0z} = f_0/(1+z)$, using the angular averaged signal-to-noise ratio (2) and signal waveform (5):

$$d_L(m_{1z}, m_{2z}, f_{0z}) = \frac{\sqrt{85} \, \pi^{2/3}}{2^{5/3}} \frac{G^{5/3}}{c^4} \frac{\mathcal{M}_z^{5/3}}{S/N} \sqrt{\frac{E_{rel}(\lambda)}{E_{nr}(\lambda)}} W(f, f_{0z}), \qquad (37)$$

where $E_{rel}(\lambda)/E_{nr}(\lambda)$ is the enhancement of the GW energy for general relativistic orbits (Gair, Kennefick, & Larson 2005, and see § 3 above), where $\lambda = \lambda(M, f_0) = \lambda(M_z, f_{0z})$ is given by eq. (30), and $W(f, f_{0z})$ is a factor depending on only

[11] We follow to notation of Miller (2002) and Will (2004) for the definition of partial event rates by not including the mass distribution $g_{CO}(m)$. The mass distributions enter only when integrating for the total event rates eq. (42).

the frequencies

$$W(f, f_{0z}) = \sqrt{\frac{4}{5} \int_{f_{min}}^{f_{max}} \frac{f_{0z}^{4/3}}{f^2} \frac{F(f/f_{0z})}{S_n(f)} \, df} \qquad (38)$$

$F(x)$ is the dimensionless, normed GW energy spectrum defined in § 3, f_{min} and f_{max} are the minimum and maximum frequencies specific for GW detectors (see § 2). Henceforth we shall fix $S/N = 5$, but other values can be roughly obtained by scaling the final result on detection rates with $(S/N)^{-3}$ (assuming that the number of sources increases with d_{Lmax}^3).

Note that eq. (37) formally depends on redshifted parameters. However, since both the differential encounter event rate (36) and the GC model mass distribution depend on the comoving parameters, it is useful to revert to the comoving parameters in eq. (37) and get $d_L(m_1, m_2, f_0)$. This can be achieved by writing $m_{iz} = (1+z)m_i$ for $i = \{1, 2\}$ and $f_{0z} = f_0/(1+z)$ in (37) and making this equal to the standard formula $d_{Lcos}(z)$ connecting the luminosity distance and redshift in a specific cosmology (e.g Eisenstein 1997, the index "cos" refers to the cosmological luminosity distance–redshift formula in order to distinguish this from the maximum distance (37) specific for PE encounters). Now both sides depend on z. Numerically solving for z gives $z(m_1, m_2, f_0)$. Finally substituting the result back in $d_{Lcos}(z)$ gives $d_L(m_1, m_2, f_0)$.

This procedure is however cumbersome in practice. It becomes numerically very time-consuming when computing the total detection rates, which includes the evaluation of integrals over the parameters. Therefore we make the following essential approximations when solving for the luminosity distance in (37):

$$d_L(m_1, m_2, f_0) \equiv \begin{cases} \text{using } z = 0 & \text{if } z_1 \leq 0.01 \\ \text{using } z = H_0 d_L/c & \text{if } z_1 \leq 0.1 \\ \text{no approximations} & \text{if } 0.1 < z_1 < 6 \\ \text{using } z = 6 & \text{if } S/N > 5 \text{ for } z = 6 \end{cases}$$
$$(39)$$

On the RHS of eq. (39), z_1 is the first approximation of the redshift, which is obtained by calculating d_L from the RHS of eq. (37) with no redshift, and making this equal to $d_{Lcos}(z_1)$, and solving for z_1. We neglect cosmology for $z_1 < 0.01$ and take a Hubble constant $H_0 = 70\,\text{km/s/Mpc}$ for $0.01 < z_1 < 0.1$. Next, whenever $z_1 > 0.1$, we substitute $z = 6$ for the RHS of eq. (37) and in case this is already larger than $d_{Lcos}(6)$, then we conclude that the source is observable at $z = 6$ for $S/N > 5$ and take $d_L = d_{Lcos}(6)$ as the maximum distance of observation. We do not explore detection rates at larger redshifts, since then the BH mass and radial distribution might not have relaxed to the final state. If $S/N < 5$ for $z = 6$ then we execute the exact procedure without approximations for $z_1 > 0.1$

Changing to the non-redshifted variables in Eq. (37) is even ambiguous in some cases. For *NGLISA* the signal-to-noise ratio is occasionally not a decreasing but an increasing function of the redshift. This happens when the signal is redshifted to the more sensitive range of frequencies of the detector, and the enhancement in sensitivity is more substantial than the attenuation from increasing the distance. In these cases a certain encounter can be observed within a certain distance, then increasing the distance, the encounter first becomes invisible (i.e. $S/N < 5$), then again visible (i.e. $S/N \geq 5$) within a second maximum distance. This phenomenon occurs for *NGLISA* for large BH masses and near-maximum characteristic frequencies.

Fig. 4 shows the maximum distance of sources with $S/N = 5$ for $m_1 = m_2 = 40 M_\odot$ BH masses. The thick curves account for
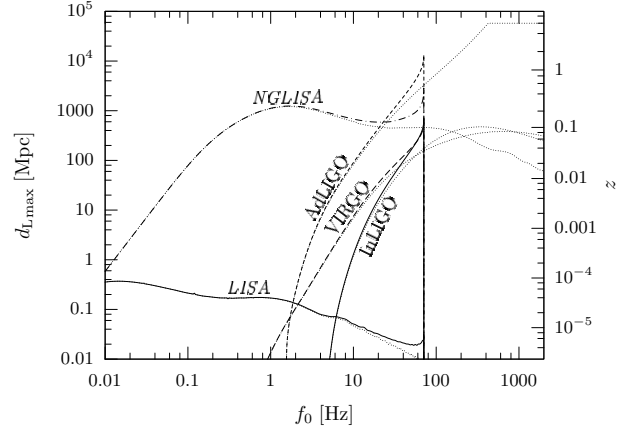

FIG. 4.— Maximum luminosity distance, d_{Lmax}, of two BHs with $m_1 = m_2 = 40 M_\odot$ masses undergoing a PE, and emitting GWs that are detected on average with $S/N = 5$. The x-axis shows the emitted f_0 characteristic frequency of the flyby comoving with the host GC. The curves correspond to InLIGO, VIRGO, AdLIGO, *LISA*, and *NGLISA*, respectively. Thin dotted lines show the result for Newtonian waveforms (Turner 1977), thick lines account for general relativistic corrections to the GW amplitudes for close encounters. For frequencies larger than $f_{M,max} = 71\,\text{Hz}$ the minimum distance is under $\lambda = 2$ Schwarzschild radii, for which a head-on collision takes place. We did not impose any restrictions on λ for the non-relativistic curves. All curves account for the redshifting z, which is shown on the right border. We restrict to $z \leq 6$. For different masses, d_L scales with roughly $\mathcal{M}^{5/3}$ and the cutoff frequency scales with M^{-1}. Since signals are broadband, the detectors have a chance to observe a broad range of f_0.

the relativistic corrections with minimum separations larger than $\lambda = 2$, the thin dotted lines represent the non-relativistic results with no bound on λ. The maximum frequency (32) corresponding to marginally colliding orbits ($\lambda = 2$) is 71 Hz and scales with M^{-1} for other masses. For other masses d_{Lmax} scales with $\mathcal{M}^{3/5}$. All curves account for the cosmological redshifting. The plot shows, that the non-relativistic approximation is adequate for small frequencies, but it implies a luminosity distance a factor of $2 - 3$ lower than the relativistic calculation near the maximum f_0 frequency. Therefore, the dotted lines are useful to approximately visualize d_{Lmax} for lower M, when the cutoff frequency shifts to higher values.

The enclosed volume and the observable sources are given by eq. (8). If neglecting relativistic and cosmological effects, we get $V \propto D^3 \propto \mathcal{M}^5$.

5.4. *Detection Rates*

In the previous sections we calculated the differential event rates of PEs for single GCs per infinitesimal mass and frequency bins, and computed the maximum distance of their detection. Here we combine these results to calculate the total detection rate of PEs.

For fixed m_1, m_2, and f_0, the rate of GW detections of the corresponding encounters is the observed rate for a single GC times the number of observable GCs. Since there is a cosmological redshift between the source GC and the observation, the single-GC rate is reduced by $1 + z$:

$$\frac{\partial^2 \nu^{total}}{\partial m_1 \partial m_2 \partial \ln f_0} = \frac{1}{1+z} \frac{\partial^2 \nu^{single}}{\partial m_1 \partial m_2 \partial \ln f_0} N^{gc}(m_1, m_2, f_0). \quad (40)$$

The first term is the redshifted event rate expressed with the comoving event rate (36) and the second is simply

$$N^{gc}(m_1, m_2, f_0) = N^{gc}[d_{Lmax}(f_0, m_1, m_2)], \qquad (41)$$
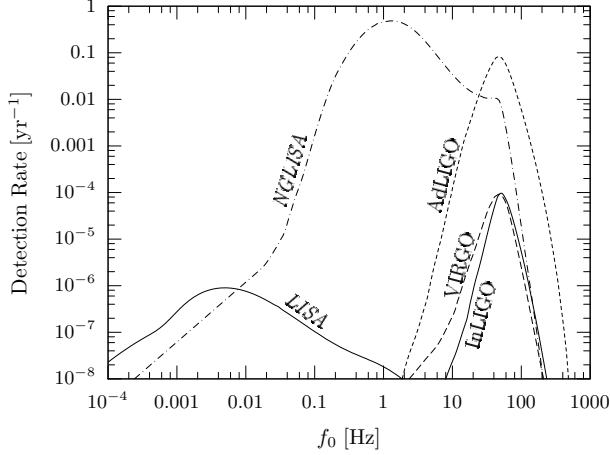
FIG. 5.— The expected PE detection rate per logarithmic emitted characteristic frequency bin. Results are shown for the specific detectors. All curves account for general relativistic encounters and cosmology. The units on the y-axis is simply yr^{-1}, since it is a rate per $\mathrm{d}\ln f_0 = \mathrm{d}f_0/f_0$ bins for which the units of f_0 drops out. For large f_0, there is an abrupt cutoff in the detection rate as the larger mass BHs suffer head-on collisions, leaving only the contribution of low-mass BHs in the PE rate.
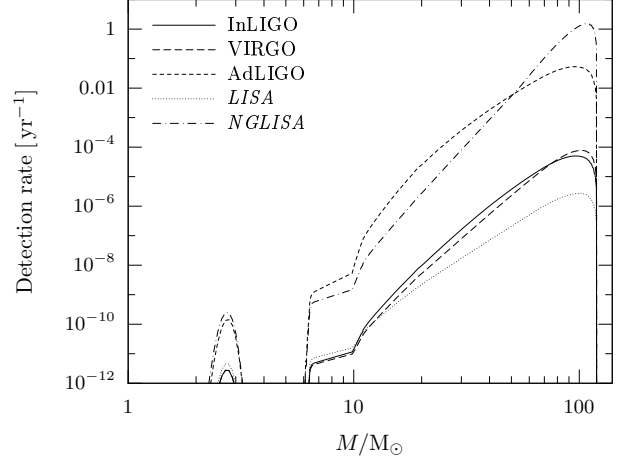

FIG. 6.— The expected PE detection rate per logarithmic total mass bins, $\mathrm{d}\ln M$, for the various detectors. Note that the mass function of our GC model is constant for $\mathrm{d}\ln m$ intervals for BHs $120\mathrm{M}_\odot > 2m > 10\mathrm{M}_\odot$, and is Gaussian type for NSs $2m \sim 2.7\mathrm{M}_\odot$. BH–NS encounters dominate for $6.35\mathrm{M}_\odot < M < 10\mathrm{M}_\odot$. The dominant PE contribution is expected from $m_{1,2} = 40-60\mathrm{M}_\odot$ component masses.

where $N^{\mathrm{gc}}(d_{\mathrm{L}})$ is the number of GCs within a given maximum luminosity distance. In practice d_{Lmax} is given by eq. (39) which we substitute in eq. (8).

The total detection rate is then simply the integral of the differential detection rate (40) using the CO mass distribution. After substituting, we get

$$\nu^{\mathrm{tot}}(f_0) = \int_0^{f_{0\max}} \frac{\mathrm{d}f_0}{f_0} \iint_{f_0 \le f_{M,\max}} \mathrm{d}m_1 \mathrm{d}m_2$$
$$g_{\mathrm{CO}}(m_1)\, g_{\mathrm{CO}}(m_2) \frac{\partial^2 \nu^{\mathrm{total}}}{\partial m_1 \partial m_2 \partial \ln f_0} \qquad (42)$$

where $g_{\mathrm{CO}}(m)$ is the CO mass distribution for Model II, defined in § 4.3.2. The mass integrals are evaluated over the (m_1, m_2) domain for which the encounter avoids a collision (i.e. $f_0 \le f_{M,\max}$, see eq. [32]) and the f_0 integral extends to a maximum possible frequency independent of masses ($\sim f_{2m_{\mathrm{NS}},\max}$). The result of eq. (42) is one number, the expected rate of detection for the specific detector.

5.5. Results

The estimated total number of successful detections from eq. (42) is $\nu^{\mathrm{tot}} = 5.5 \times 10^{-5}\,\mathrm{yr}^{-1}$ for InLIGO, $7.2 \times 10^{-5}\,\mathrm{yr}^{-1}$ for VIRGO, $6.3 \times 10^{-2}\,\mathrm{yr}^{-1}$ for AdLIGO, $2.9 \times 10^{-6}\,\mathrm{yr}^{-1}$ for *LISA* and $1.0\,\mathrm{yr}^{-1}$ for *NGLISA*.

It is interesting to see the differential event rate per logarithmic f_0 bin independent of masses, which is obtained by carrying out only the mass integrals in eq. (42). The result is shown in Fig. 5. The figure shows that both AdLIGO and *NGLISA* could have some chance to detect PE events, if observing for one year; AdLIGO mainly sensitive to f_0 frequencies between 30 and 80 Hz, and *NGLISA* sensitive between 0.2 Hz and 10 Hz. There is a sharp cutoff in the PE detection rate for high frequencies. In this regime, the encounters among the relatively higher mass BHs are not parabolic, but result in direct captures, and only the lower mass BHs contribute to the PE detection rate. show the differential event rate for logarithmic total mass bins, $\mathrm{d}\ln M$, and for logarithmic mass ratio bins, $\mathrm{d}\ln q$. Here we define the mass ratio as $q = m_</m_>$ for which $q \le 1$. (Recall the definitions $m_< = \min(m_1, m_2)$

and $m_> = \max(m_1, m_2)$.) The M dependent partial PE detection rate can be obtained from eq. (42) by changing the m_1, m_2 integrals to M and m_2 variables, rearranging the order of integrals, and evaluating the f_0 and m_2 integrals only. The partial PE rates for fixed q can be obtained similarly, by changing to $m_>$ and q variables, and evaluating the f_0 and $m_>$ integrals only. In § 5.1.2 we demonstrated that the event rates of GCs are sensitive to $\langle m^{10/3} \rangle$, and are inclined towards the high-mass end of the CO distribution, in particular PEs of NSs have a relatively negligible event rate. The detectable volume entails an even stronger mass dependence m^5. Therefore, for a mass distribution of m^{-1}, we expect a scaling with $\sim m^{22/3}$ for logarithmic total mass bins, implying that the highest mass BHs will dominate the PE event rates. However, increasing the BH masses decreases the maximum f_0 frequency of an encounter avoiding a collision. Figure 6 verifies that all of the detectors are indeed much more sensitive to large total masses, even though our model GC (i.e. Model II) contains a small relative number of these objects. Note, that the BH mass distribution $g_{\mathrm{BH}}(m)$ is constant for $\mathrm{d}\ln m$ bins. With Figure 6 the partial detection rates of BH–BH and NS–NS encounters can be visualized. For $M > 2m_{\min} = 10\mathrm{M}_\odot$ the BH–BH encounters dominate, while $M \approx 2m_{\mathrm{NS}}$ correspond exclusively to NS–NS encounters. PE detections of NS–NS encounters are practically impossible, they are suppressed by at least 9 orders of magnitudes. Similarly, Figure 7 shows that BH–NS encounters are also suppressed by 6 orders of magnitudes!

Figure 8 shows the detection rate as a function of minimum distance, $\lambda_{\min}$ of the encounters. Recall that for a given total mass M, λ determines the characteristic frequency f_0 by eq. (33), and marginally plunging orbits correspond to $\lambda_{\min} = 2$. Figure 8 was obtained by changing the domain of integration of f_0 to $f_0 \lesssim f_{M,\lambda}$ in eq. (42). The curves show that terrestrial detectors are more sensitive to close approaches than space detectors. The $\lambda_{\min} = 2$ case corresponds to all of the PE detections. It is interesting to note, that terrestrial detectors display a different λ dependence: AdLIGO rates show a weaker increase for marginally colliding orbits $\lambda \sim 2$. This is a consequence of cosmology: the observation distance is so large (Fig. 4) that the cosmological comoving volume element
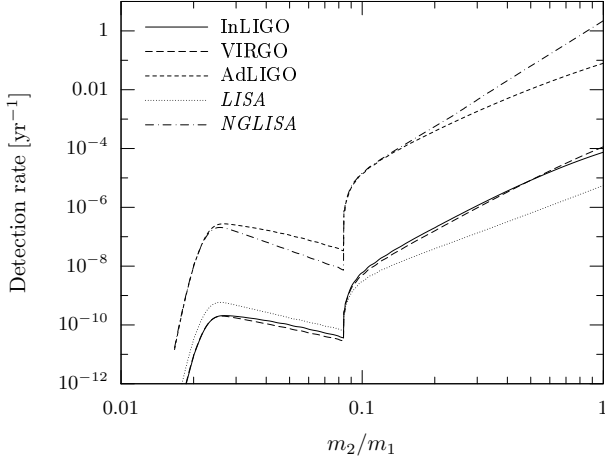
FIG. 7.— The expected PE detection rate as a function of the mass ratio $q = m_2/m_1$ of the interacting masses, where $m_1 \geq m_2$ is assumed. The partial PE detections are plotted per logarithmic mass ratio bins, $d \ln q$, for the various detectors. Note that the assumed smallest and largest CO masses of our GC model implies a cutoff below $1.35M_\odot/60M_\odot$. The detection rate is dominated by equal mass encounters. PEs with $q > 5M_\odot/60M_\odot$ are dominated by BH–BH encounters, while $1.35M_\odot/60M_\odot \lesssim q < 5M_\odot/60M_\odot$ correspond to BH–NS events.
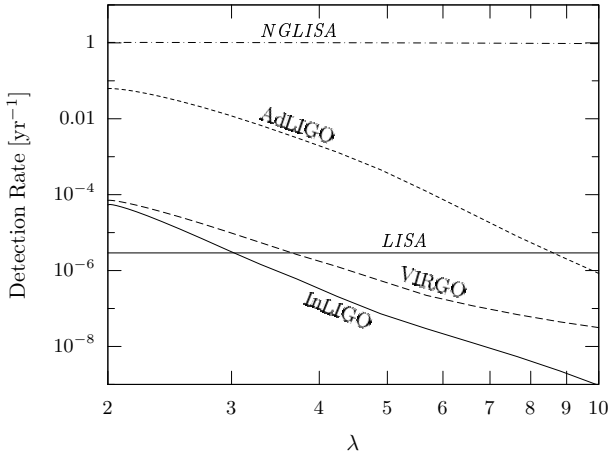

FIG. 8.— The total cumulative expected detection rate of PEs subject to the constraint that the minimum separation exceeds λ times the total Schwarzschild radius. For $\lambda < 2$ a head-on collision occurs, which we are not considering in the present paper (see § 7.1 for a discussion).

TABLE 1
DETECTION RATES FOR ALTERNATIVE MODELS

p	$m_{\max}$ [M$_\odot$]	$m_{\min}$ [M$_\odot$]	ν_{InLIGO} [yr^{-1}]	ν_{VIRGO} [yr^{-1}]	ν_{AdLIGO} [yr^{-1}]	ν_{LISA} [yr^{-1}]	ν_{NGLISA} [yr^{-1}]
0	20	5	1.0(−6)	5.2(−7)	2.2(−3)	8.7(−8)	6.3(−4)
0	60	5	2.2(−4)	3.1(−4)	2.4(−1)	1.2(−5)	5.2
0	60	40	1.3(−4)	2.1(−4)	1.3(−1)	7.2(−6)	4.3
0	100	5	1.0(−3)	3.6(−3)	1.3	1.3(−4)	
0	100	40	9.5(−4)	3.4(−3)	1.2	1.2(−4)	
0	100	80	2.4(−4)	1.2(−3)	3.4(−1)	4.3(−5)	
1	20	5	4.8(−7)	2.4(−7)	1.0(−3)	4.5(−8)	2.7(−4)
1	**60**	**5**	**5.5(−5)**	**7.2(−5)**	**6.3(−2)**	**2.9(−6)**	**1.0**
1	60	40	2.5(−5)	3.9(−5)	2.6(−2)	1.3(−6)	7.6(−1)
1	100	5	2.2(−4)	6.4(−4)	2.8(−1)	2.4(−5)	
1	100	40	1.8(−4)	5.7(−4)	2.2(−1)	2.0(−5)	
1	100	80	2.9(−5)	1.4(−4)	4.2(−2)	5.2(−6)	
2	20	5	1.8(−7)	9.1(−8)	4.1(−4)	2.1(−8)	9.5(−5)
2	60	5	6.6(−6)	7.2(−6)	8.3(−3)	3.7(−7)	8.4(−2)
2	60	40	1.8(−6)	2.8(−6)	1.9(−3)	1.0(−7)	5.0(−2)
2	100	5	1.7(−5)	3.6(−5)	2.1(−2)	1.5(−6)	
2	100	40	9.7(−6)	2.7(−5)	1.1(−2)	9.6(−7)	
2	100	80	8.9(−7)	4.3(−6)	1.3(−3)	1.6(−7)	

NOTE. — The number of BHs per GC is normalized to $N_{\mathrm{BH}} = 500$ for $m_{\min} = 5M_\odot$ for all choices of $m_{\max}$. For larger $m_{\min}$, all BHs with $5M_\odot \leq m < m_{\min}$ are assumed to have escaped from the cluster. Detection rates are given in normal form, where the exponent is shown in parenthesis. Some fields left blank correspond to cases where the S/N is not a monotonically decreasing function of distance (see § 5.3).

sults for these models. Here, we have fixed $N_{\mathrm{BH}} = 500$ for models with $m_{\min} = 5M_\odot$. For larger $m_{\min}$, we reduce N_{BH} by assuming that BHs with masses $5M_\odot \leq m < m_{\min}$ have escaped the cluster. Results are very different for various choices of parameters (see § 7.3.2 for a detailed discussion below).

We constructed two different GC models. We conclude that a uniform mass and density distribution (Model I) is inadequate since the contribution of the GC core consisting of the more massive BHs are significantly underestimated. After accounting for mass distribution and mass segregation, as well as the relative velocity distribution of the sources (Model II) we obtained event rates two orders of magnitudes higher than Model I per GC. Moreover, more massive BHs in GCs are visible to significantly larger distances, and supply the most prominent sources of PEs for detection (Fig. 6).

In § 7, we include a critical review of our assumptions and their influence on the results. To point out just one thing, note that compared to our previous estimates above, the PE detection rates might have been underestimated by four orders of magnitudes for core-collapsed GCs (depending on the final core radius and population, see § 7.3.3 below)!

7. DISCUSSION

7.1. *Comparison with Other Orbits*

How do PE event rates compare to the event rates of binary inspirals, mergers, and head-on collisions? What are the main factors for the difference? We briefly discuss these questions in this section.

is significantly smaller, and the GW frequency is redshifted outside the sensitive domain of the detector for these events.

6. CONCLUSIONS

PEs of solar BHs are possible sources of gravitational radiation. Our results suggest that current and near future GW detectors are potentially capable of detecting these signals in the local universe and up to cosmological distances for the higher masses. We anticipate $S/N \gtrsim 5$ matched-filtering detection rates for quasi-parabolic trajectories avoiding collisions, $\nu^{\mathrm{tot}} = 5.5 \times 10^{-5}\,\mathrm{yr}^{-1}$ for InLIGO, $7.2 \times 10^{-5}\,\mathrm{yr}^{-1}$ for VIRGO, $0.063\,\mathrm{yr}^{-1}$ for AdLIGO, $2.9 \times 10^{-6}\,\mathrm{yr}^{-1}$ for *LISA*, and $1.0\,\mathrm{yr}^{-1}$ for *NGLISA*. For different signal-to-noise ratios, detection rates scale by approximately $(S/N)^{-3}$. These results correspond to a BH mass function $g_{\mathrm{BH}}(m) \propto m^{-1}$ with minimum and maximum masses of 5 and $60M_\odot$. For comparison we ran calculations for more general distributions $g_{\mathrm{BH}}(m) \propto m^{-p}$, and different $m_{\min}$ and $m_{\max}$ values. Table 1 lists the re-

7.1.1. *Basic Features of Parabolic Encounters*

Let us quickly summarize the main properties of PE sources.

• The event rates for $d \ln f_0$ intervals scale with $f_0^{-2/3}$ for trajectories avoiding collisions. Collisions decrease PE

event rates quickly for large frequencies, $f \gtrsim 50\,\mathrm{Hz}$, rates drop four orders of magnitudes between 50 and 500 Hz.

- The f_0-scaling of the amplitude of the signal is $f_0^{-1/3}$ for GW frequencies $f \sim f_0$. The integrated RSS signal amplitude scales with $f_0^{1/6}$.

- The signal energy-spectrum is broadband, has a maximum at $f \sim f_0$, and a relatively shallow cutoff for larger frequencies. The half-maximum of the signal is $\Delta f \sim 1.5 f_0$, and the spectral energy density drops to 1% at $f \sim 5 f_0$ (Turner 1977).

- In terms of detections for $d\ln f_0$ intervals, the maximum distance of PE detections for a band-pass detector is roughly independent of frequencies between $f_{\min} \lesssim f_0 \le f_{0\,\max}$, where $f_{\min}$ is the minimum detectable frequency of the detector and $f_{0\,\max}$ is the maximum characteristic frequency of a PE avoiding collisions.

- The detection rates of equal-mass PEs scale with $\langle m^{22/3} \rangle$ for $d\ln m$ intervals, the higher mass BHs dominate PE detections.

- Space detectors will possibly detect more PE events in the local universe, but terrestrial detectors see further.

- Typical event rates are $1.6 \times 10^{-12}\,\mathrm{yr^{-1}GC^{-1}}$ or equivalently $\mathcal{R} = 1.4 \times 10^{-11} h^3\,\mathrm{yr^{-1}\,Mpc^{-3}}(\Delta \ln f_0)^{-1}$ for $f_0 = 50\,\mathrm{Hz}$.

- Typical maximum distance of detection for PEs *with appropriate* f_0 is $\sim 300\,\mathrm{Mpc}$ for InLIGO and VIRGO, $z \sim 1$ for AdLIGO, $\sim 0.4\,\mathrm{Mpc}$ for *LISA*, and $z \sim 0.2$ for *NGLISA*.

- Typical overall rate of PE detections per year is $\sim 10^{-4}$ for InLIGO and VIRGO, ~ 0.1 for AdLIGO, $\sim 10^{-6}$ for *LISA*, and ~ 1 for *NGLISA*.

Table 2 contrasts the event rates of PEs and other possibly detectable sources in the literature. The event rates, $\mathcal{R}$, listed in the table are normalized to an average space density of galaxies $n_{\mathrm{gal}} = 0.029\,\mathrm{Mpc^{-3}}$ and $n_{\mathrm{gc}} = 2.9\,\mathrm{Mpc^{-3}}$ for GCs (see § 4.2). For PEs the $\mathcal{R}$ values shown correspond to the sensitive range of characteristic frequencies: $10\,\mathrm{Hz} \le f_0 \le 200\,\mathrm{Hz}$ for InLIGO, VIRGO, AdLIGO, $10^{-4}\,\mathrm{Hz} \le f_0 \le 1\,\mathrm{Hz}$ for *LISA*, and $10^{-1}\,\mathrm{Hz} \le f_0 \le 60\,\mathrm{Hz}$ for *NGLISA* (see Fig. 5). The maximum distance of detection, d_{L}, shown are typical values for detectable encounters. The elements marked with "-" are not given by the corresponding references. Values are left blank that are the same as in the previous row. Note that the numbers are very uncertain depending on model assumptions. PE event rates correspond to our standard GC model, most significant uncertainties are the numbers of higher mass BHs in the cluster. Note, that stellar BH–BH inspiral event rate estimates in GCs vary 3 orders of magnitudes!

7.1.2. *Parabolic Encounters vs. Inspirals*

The event rates of PEs depend on the characteristic frequency. Without any specifications PEs are more regular than e.g. BH–BH inspirals. However, *within the sensitive range* of GW terrestrial detectors PEs are rather rare by a factor of $\sim 10^{-4}$. Event rates are higher for space detector frequencies,

TABLE 2
COMPARISON OF EVENT AND DETECTION RATES WITH OTHER SOURCES

Event	Loc	$\mathcal{R}$	Detector	d_{L} [Gpc]	ν [yr^{-1}]
BH/BH PE[1]	GC	7.1(−11)	InLIGO	3.0(−1)	5.5(−5)
	GC	7.1(−11)	VIRGO	3.0(−1)	7.2(−5)
	GC	7.1(−11)	AdLIGO	5.6	6.3(−2)
	GC	2.4(−7)	*LISA*	5.1(−4)	2.9(−6)
	GC	2.4(−9)	*NGLISA*	1.9	1.0
NS/NS insp[2]	Field	1.9(−7)	AdLIGO	2.0(−1)	3.0
([3]LPP)	Field	1.1(−6)	AdLIGO	2.0(−1)	3.4(+1)
([4]Kalogera)	Field	2.0(−6)	InLIGO	2.0(−2)	3.5(−2)
		2.0(−6)	AdLIGO	3.5(−1)	1.9(+2)
([5]NGF)	Field	2.9(−4)	InLIGO	2.0(−2)	3.4(−1)
		2.9(−4)	AdLIGO	3.0(−1)	1.1(+4)
BH/NS insp[5]	Field	2.9(−4)	InLIGO	4.3(−2)	3.3(+1)
		2.9(−4)	AdLIGO	6.5(−1)	1.2(+5)
BH/BH insp[6]	Field	2.0(−9)	AdLIGO	1.1	1.0
([7]PZM)	Nucleus	1.8(−8)	AdLIGO	1.1	1.0(+2)
	Zero-age GC	3.2(−7)	AdLIGO	1.1	1.8(+3)
	Evolved GC	5.4(−8)	AdLIGO	1.1	3.0(+2)
([8]Miller)	GC	3.5(−9)	AdLIGO	1.6	1.0(+1)
([9]O'Leary)	Zero-age GC	8.7(−7)	AdLIGO	−	2.7(+3)
	Evolved GC	8.7(−10)	AdLIGO	−	2.7
IMBH/BH[8]	GC	3.5(−9)	AdLIGO	1.6	4.0(+1)
		3.5(−9)	*LISA*	2.0(−1)	7.0(−3)
([10]Will)	GC	8.5(−9)	*LISA*	4.0(−2)	1.0(−6)
([11]GMH)	GC	5.1(−5)	*LISA*	4.0(−2)	6.0(−3)
([12]HPZ)	Field	1.4(−7)	*LISA*	3.5(−1)	8.6
SMBH/WD[13]	Nucleus	1.7(−8)	*LISA*	1.6	9.4(+1)
([14]HA)	Nucleus	9.0(−8)	*LISA*	1.0	1.3(+2)
SMBH/BH[13]	Nucleus	3.2(−9)	*LISA*	6.6	1.1(+3)
SMBH/IMBH[13]	Nucleus	2.9(−12)	*LISA*	6.6	1.0
([15]PZ)	Nucleus	8.3(−10)	*LISA*	4.4	1.0(+2)

NOTE. — Event rates $\mathcal{R}$ are in units $h^3\mathrm{yr^{-1}Mpc^{-3}}$.

[1] Parabolic encounters for our standard GC model. The maximum distance of detection corresponds to $m_1 = m_2 = 50\mathrm{M_\odot}$, $f_0 = 50\,\mathrm{Hz}$ for InLIGO, VIRGO, AdLIGO and *NGLISA*, and $f_0 = 10\,\mathrm{mHz}$ for *LISA*.

[2] NS/NS inspirals, Portegies Zwart & Spreeuw (1996) theoretical models of binary evolution calibrated to the observed supernova rate.

[3] Lipunov, Postnov, & Prokhorov (1997)

[4] Kalogera et al. (2004), based on 3 highly relativistic radio pulsars.

[5] Nakar, Gal-Yam, & Fox (2005), based on recent observations of 4 short/hard gamma-ray bursts, identified with NS/NS or BH/NS inspirals.

[6] BH/BH inspirals, Portegies Zwart & Yungelson (1998).

[7] Portegies Zwart & McMillan (2000). Distance corresponds to the inspiral of masses $m_1 = m_2 = 10\mathrm{M_\odot}$ and detection rates correspond to a 100% detection efficiency within this distance.

[8] Miller (2002)

[9] O'Leary et al. (2006). They compute the number of mergers as a function of time, as BHs are being slowly depleted from the cluster. The detection rates correspond to cases, where all GCs are zero-age (1 Myr) or evolved (10 Gyr), with a number density $1\,\mathrm{Mpc^{-3}}$.

[10] Stellar BH inspirals into intermediate mass BHs, adopted from Will (2004). Distance corresponds to the inspiral of masses $m_1 = 100\mathrm{M_\odot}$ and $m_2 = 10\mathrm{M_\odot}$, $\mathcal{R}$ corresponds to the inspirals with a maximum time 40–400 yr before merger which can be detected with $S/N = 10$ after a 1 yr integration with *LISA*.

[11] Gültekin, Miller, & Hamilton (2006) assuming more optimistic probability of IMBHs in GCs and IMBH maximum mass than Will (2004)

[12] Hopman & Portegies Zwart (2005), assuming observed ultraluminous X-ray sources are associated to tidal captures of $10\mathrm{M_\odot}$ BHs by $10^3\mathrm{M_\odot}$ IMBHs.

[13] Inspirals into supermassive BHs, $M = 10^6\mathrm{M_\odot}$. Gair et al. (2004) assuming their optimistic set of results.

[14] Hopman & Alexander (2005)

[15] Portegies Zwart et al. (2006) N-body simulations of the formation and inward migration of IMBHs in the Galactic center.

however space detectors have a smaller distance of maximum observation.

Table 2 suggests that the detectable distance of PEs is comparable to inspirals. However, this is somewhat deceptive since PE results correspond to larger BH masses, $50 M_\odot$ rather than $10 M_\odot$ which is regular for BH–BH inspirals in the literature. For $10 M_\odot$ component masses, the maximum distance of observation is less for PEs than for inspirals (Fig. 4), the PE event rates are suppressed by a factor of $\sim 10^3$ (Fig. 6). However for larger masses the comparison changes with the following factors. First, although the GW signal amplitude is proportional to $\mathcal{M}^{5/3}$ for inspirals, increasing the masses reduces the signal frequency (which in turn reduces the detector sensitivity) and also reduces the observation time (which also decreases the effective signal amplitude). Another important difference is in the binary separation λ which determines the signal frequency. It is restricted to $\lambda > 3$ for inspirals, the innermost stable circular orbit, a more stringent constraint than the condition $\lambda > 2$ for PEs (see § 5.2). Finally opposed to the PE signal waveforms, the inspiral signals are narrow band, implying that the high mass, i.e. low frequency, inspiral waveforms are much harder to detect as much smaller signal power accumulates at the more sensitive range of frequencies. When combining all of these effects we expect that low mass BH inspirals are detectable further with terrestrial detectors, while for large masses where the observation is limited to at most a few orbits, marginally collisional PEs are better detected. Therefore, detectors can observe the higher mass encounters for PEs. This is exactly analogous to the comparison of the inspiral and plunge phases of binary coalescence, for which the detection of plunge dominates for large masses (Flanagan & Hughes 1998).

Among the GW detection candidate sources in GCs, PEs are very infrequent compared to stellar BH–BH inspiral rate estimates of Portegies Zwart & McMillan (2000) or Miller (2002) within GCs, but are comparable to the recent results of O'Leary et al. (2006). Observations of radio pulsars and gamma ray bursts suggest several orders of magnitude larger numbers for NS–NS or BH–NS inspiral detections (Kalogera et al. 2004; Nakar, Gal-Yam, & Fox 2005).

7.1.3. *Parabolic Encounters vs. Head-on Collisions*

As a second example, let us consider the event rates of head-on collisions for unbound encounters. Head-on collisions are related to PEs, by extending the parameter λ to values less than 2, the unstable circular orbit. Thus it would be relatively straightforward to extend the analysis to these events, by examining the event rates for small initial impact parameters, and computing the detectability as a function of this parameter. However, the exact shapes of gravity waveforms are presently not available for collisions (see Baker et al. 2006 for current progress), therefore maximum likelihood detections are not possible, and the detection of these bursts requires much higher signal-to-noise levels. We shall argue that direct head-on collision detections are potentially less frequent than PEs.

The rate of head-on collisions between BHs is well known (e.g Hills & Day 1976; Cutler, Kennefick, & Poisson 1994; Sigurdsson & Rees 1997) however the detection rates of the resultant GW signals is subject to the uncertainty of the GW signals (Flanagan & Hughes 1998). Direct collisions produce potentially less intensive GW signals than close PEs even if neglecting the relativistic amplitude enhancement for PEs. To see this, let us compare GW signal strengths that we adopt

for PEs (see § 3, and Turner 1977; Martel 2004; Gair, Kennefick, & Larson 2005), with general relativistic calculations for head-on collisions. To our best knowledge, off-axis collisions of BHs have not been calculated as a function of impact parameter. For radial head-on collision of Schwarzschild BHs $\Delta E \simeq 0.01 \, (\mu^2/M) c^2$ (Davis et al. 1971; Anninos et al. 1993; Moreschi 1999; Sperhake et al. 2005). Sasaki & Nakamura (1982) derived GW energies for the radial infall of a test particle into a Kerr BH, and Mine, Shibata, & Tanaka (1996) accounted for the spin of the infalling particle in addition. Results are in the range of $\Delta E = 0.03 - 0.01 \, (\mu^2/M) c^2$ according to the magnitude and alignment of spins and the relative direction of the approach. For high-velocity head-on collisions, there are significantly larger results: $\Delta E = 0.328 \, \mu c^2$ for non-rotating BHs (D'Eath & Payne 1992), and up to $\Delta E = 0.70 \, \mu c^2$ for extreme Kerr-BHs (Cardoso & Lemos 2003). However, in GCs the initial velocities are typically non-relativistic, therefore we do not expect a significant relative contribution of relativistic head-on collisions. Once the BHs are so near that a common surrounding horizon envelope forms the space-time relaxes to a Kerr-BH. The energy output of this process is between $\Delta E = 6 \times 10^{-6} M c^2$ (Price & Pullin 1994) for axisymmetric encounters and $\lesssim 0.01 M c^2$ for quasi-circular initial conditions (Khanna et al. 1999). In comparison, the energy output in GWs for non-relativistic PEs is $\Delta E_{\rm PE} = 0.01 \, (\lambda/4.1)^{-7/2} (\mu^2/M) c^2$ (Turner 1977). Using the low-velocity case, the GW amplitudes of BH collisions are overestimated by the Newtonian results by a factor between $(\lambda/3)^{-7/2}$ and $(\lambda/4)^{-7/2}$, depending on spins. Therefore, the extapolation of the Newtonian treatment to the regime where the minimum separation is $\lambda \ll 3$ leads to significant overestimates of the true head-on collision GW energies. In conclusion, the extrapolation of event rates as a function of λ (for $\lambda < 2$ in Fig. 8) or as a function of the logarithmic characteristic frequency (for $f_0 > f_{\lambda=2}$ in Fig. 4, dotted lines) is possibly overly optimistic and therefore inadequate for the estimation of the detection rates of head-on collisions with the particular GW detectors.

7.2. *Approximations in the Analysis*

Our event rate estimates rely on several approximations. The most important caveat in our analysis is possibly neglecting GW recoil capture in bound eccentric orbits. The GW radiation reaction is substantial for strong gravitational fields, for low λ. For initially nearly parabolic orbits, the periastron distance and the eccentricity is decreased[12] (Cutler, Kennefick, & Poisson 1994). The first consequence is a minor decrease in the PE event rate, because of the increase of the cross-section of direct capture. On the other hand, GW recoil produces bound orbits from initially unbound trajectories (Lee 1993). The periastron distance is then further decreased during each subsequent close approach inducing successively stronger GW radiation. Therefore PE events are potential precursors of multiple subsequent more intense highly eccentric bound encounters, analogous to the captures of stellar compact objects by supermassive black holes (Hopman & Alexander 2005). The GW detection rate of the resultant orbits is likely to be significantly higher than PE detections. As a result, we anticipate several successful detections for AdLIGO per year for a wide range of BH mass-distribution models (see

---

[12] unless $\lambda \gtrsim 2.05$, in which case the eccentricity is increased by GW recoil

Tab. 1 for PEs without GW recoil capture). We leave a detailed quantitative study for a future paper.

There is a second independent reason suggesting that higher detection rates will be more likely. Throughout the paper, we estimated matched filtering detection signal-to-noise amplitudes with the angular averaged formula which is valid for an analysis using only a single GW detector. However, a coincident analysis incorporating several detectors allows much more optimistic detection limits (see Jaronowski et al. 1996, and § 3 above). If lowering the angular averaged minimum detection limit to $S/N = 3/\sqrt{5}$ (equivalent to an optimal-orientation single-detector observation at $S/N = 3$) yields $\nu^{tot} = 1.7 \times 10^{-3} \, \text{yr}^{-1}$ for InLIGO, $2.7 \times 10^{-3} \, \text{yr}^{-1}$ for VIRGO, $0.46 \, \text{yr}^{-1}$ for AdLIGO, and $9.5 \times 10^{-6} \, \text{yr}^{-1}$ for *LISA* for our standard GC Model II with $N_{BH} = 500$, $p = 1$, $m_{min} = 5 M_\odot$, and $m_{max} = 60 M_\odot$. For models with larger m_{max} detection rates are even higher (see Tab. 1), implying several successful detections per year for advanced terrestrial detectors.

We have also neglected the bound binary interactions in the scattering dynamics and restricted only to single-single encounters. Depending on the angle of injection this could increase or decrease event rates. However our analysis of single–single interaction shows (§ 5.1.2), that the typical numerical values for PE cross-sections are extremely small, so that the injection has to have an initial velocity very accurately pointed towards the target CO in order to produce a detectable signal. For typical encounters with $m_1 = m_2 = 50 M_\odot$ and $f_0 = 50 \, \text{Hz}$, the minimum separation is $b_0 \sim 10^{-6} \, \text{AU}$, and the impact parameter is $b_\infty \sim 10^{-2} \, \text{AU}$. As a result, for single–binary interactions we speculate that the separation of scales is possible to distinguish three independent phases of the interaction: (i) the faraway zone $r \gg a_{bin}$, (ii) the intermediate zone $r \sim a_{bin}$, and (iii) the PE zone $r \sim b_0 \ll a_{bin}$. In (iii) the binary companion can be discarded. Moreover, note that the velocity during (ii) is still negligible compared to (iii). Therefore in practice, the beginning of phase (iii) is exactly analogous to the initial conditions of a single–single encounter. The only difference is the distribution of velocities is not isotropic, but after phase (i) it is beamed toward the center of mass, and phase (ii) adds a random deflection due to the companion. Plugging in the numbers for binary separations of $a_{bin} \gg 10^{-2} \, \text{AU}$ we conclude, binary focusing is not likely to significantly modify our PE rate estimates. Numerical simulations would be needed to determine the exact modifications in the estimates.

Binary interactions also alter the total number and mass distribution of BHs in the cluster. However in our calculations the total number and mass function of BHs are input parameters, which can be chosen consistently with the most sophisticated simulations.

Throughout our analysis we assumed simplified GC models. While our most sophisticated model accounts for the mass distribution, mass segregation, and relative velocities (see § 4.3) it does not consider the nonuniform radial distribution of density of regular stars in the cluster core, nor does it consider variations around the characteristic GC model parameters (e.g. virial radius, total mass, etc). However, the final results are simple powers of the characteristic parameters ($\nu \propto q^2 N_{tot}^{1.5} R^{-2.5}$). Our treatment allows upper and lower bounds to be made on the exact GC model detection rates. These bounds are still much tighter than other sources of uncertainties, which justifies the simplifying model assumptions in this analysis.

Another major approximation was to adopt the angular averaged signal waveforms in the Newtonian approximation (Turner 1977), and corrected for the relativistic enhancement of the amplitude, substantial for close-encounters. We adopted the relativistic correction for the quadrupole radiation of a test particle geodesics (Martel 2004; Gair, Kennefick, & Larson 2005) and extrapolated results for other masses. These estimates do not account for GW recoil. However, Fig. 8 shows that the contribution of extreme zoom-whirl orbits $\lambda \approx 2$ does not ruin our estimates, since the detection rate does not increase substantially for marginally plunging orbits. GW recoil reduces PE signal-power by driving the interacting masses to collisions, thereby terminating extreme zoom-whirl orbits much sooner than the no-recoil encounter time (Gair, Kennefick, & Larson 2006). We conclude that neglecting GW recoil did not lead to a large overestimate, implying that our results are acceptable approximations in this respect.

An exact treatment would have to utilize the more exact post-newtonian waveforms of the general problem using arbitrary masses and spins, and should take into account the forward peaking of GWs for high velocities, Doppler shift of GW frequencies, spin-orbit, and spin-spin interactions, etc. Although it is clear that a real data analysis matched filtering would have to be carried out with exact signal templates, the leading-order (i.e. Newtonian) term dominates the angular averaged signal power, which is therefore an adequate first estimate for the detection rates.

7.3. *Uncertainties in the Result*

7.3.1. *Model Parameters*

There are several uncertainties in our estimate. Among the most important uncertainties are the values of the GC model parameters, like the number of BHs in the cluster N_{BH}. Portegies Zwart & McMillan (2000) derives $q_{BH} = N_{BH}/N_{tot} = 6 \times 10^{-4}$ by using Scalo (1986) initial mass function (IMF) and assumed that every object more massive than $20 M_\odot$ up to $100 M_\odot$ had evolved to a BH. When using a Salpeter IMF, the result is $q_{BH} = 10^{-3}$ (Miller 2002), and Kroupa & Weidner (2003) IMF gives $q_{BH} = 1.5 \times 10^{-3}$ (O'Leary et al. 2006). We adopt the most conservative result of Portegies Zwart & McMillan (2000). However there is a chance that a non-negligible fraction of the stars have been ejected from the cluster or have undergone subsequent mergers. Both processes increase the estimate on the final BH fraction (Miller 2002). On the other hand dynamical binary interactions, binary recoil kicks, or GW recoil of BH mergers can eject BHs, thereby reducing their overall numbers and possibly also modify the mass-distribution. In fact, a significant portion of the stellar-mass BH population might be ejected, especially in small clusters (Sigurdsson & Hernquist 1993; Portegies Zwart & McMillan 2000; O'Leary et al. 2006). Belczynski et al. (2005) find that for an initial binary fraction of 50%, the retained fraction of BHs varies between 0.4 and 0.7. In our fiducial calculations we adopted $q_{BH} = 5 \times 10^{-4}$ and $N^{tot} = 10^6$. To see the effects of BH ejection, Tab. 1 shows results for other models. For the general case, we provide analytical scalings which can be readily used in case these parameters are better determined in the future. For example since $\nu^{tot} \propto N_{BH}^2$, for $N_{BH} = 5000$ (50) detection rates increase (decrease) by a factor of 100.

7.3.2. *Black Hole Mass Distribution*

An even more significant source of uncertainty is the mass distribution of BHs in the clusters. We have calculated detection rates for several distributions (Tab. 1). Increasing the p exponent of the distribution, $g_{BH} \propto m^{-p}$, decreases the detection rate by a factor of ~ 5 for a unit change in p. Changing the maximum mass of the distribution varies the results even more significantly. Compared to the detection rate corresponding to $m_{max} = 60 M_{\odot}$, for $m_{max} = 100 M_{\odot}$ ($20 M_{\odot}$) we get a $\sim 1 - 3$ order of magnitude increase (decrease) depending on the detectors. We have also tried changing the minimum mass m_{min}, by assuming that the BHs with masses $m < m_{min}$ have escaped from the cluster. Compared to $m_{min} = 5 M_{\odot}$, a value of $m_{min} = 40 M_{\odot}$ reduces detection rates by a factor of ~ 2. In the appendix, we provide ready-to-use formulas for calculating detection rates for other parameter values.

From the theoretical point of view, simulations of the initial stellar BH mass function (Fryer & Kalogera 2001) result in a maximum mass limit of $\sim 20 M_{\odot}$, but the particular form of the mass function is very different for various assumptions (fraction of explosion energy used to unbind the star, stellar winds, mass transfer after helium ignition, etc). Recent simulations of rapid star evolution assuming a lower metallicity for the progenitor stars (weaker stellar winds) appropriate for GCs and including a large fraction of binaries, collisions, and accretion leading to the mass buildup of BHs imply a stellar-mass BH distribution with maximum BH masses around $M_{max} = 60 - 100 M_{\odot}$ (Belczynski et al. 2005). Simulations of the subsequent long-term dynamical evolution has been shown to be sensitive to BH binary and triple interactions (O'Leary et al. 2006). Binary-single body interactions, BH-star collisions, and GW recoil kick can possibly significantly reduce the low mass BH population but enhance the mass of the most massive BHs in the cluster. From the observational point of view, there is yet lacking evidence for stellar mass BHs with $m > 20 M_{\odot}$, but this might be accounted for the low number statistics (a total of 20 X-ray stellar-mass BH candidates have been identified to date, Casares 2005).

7.3.3. Core Collapse

Finally, a considerable uncertainty in the PE detection rates results from the actual scaling of the mass segregation relationships. Even in our complicated model we have assumed a simple mass segregation, based on thermal equipartition among the specific CO components. This assumption is in fact valid only among the decoupled high mass components within the core. Spitzer (1969) has shown that in simple two-component systems consisting of masses m_1 and m_2, with $m_1 \ll m_2$, global equipartition cannot be attained if the low-mass component determines the potential everywhere in the cluster. In this case, the high mass components become dynamically decoupled from the rest of the cluster, and the cluster core collapses to a much smaller radius, R_{core}. This picture has been confirmed by numerical simulations for more general mass functions (Watters, Joshi, & Rasio 2000, and references therein). Gürkan, Freitag, & Rasio (2004) showed that approximate local thermal equipartition is attained within the core, and velocities follow $v_m = (Km/m_{BH})^{-1/2} v_{core}$, where v_{core} is the velocity dispersion, m_{BH} is the mass of components in the core, K describes the departure from equipartition, it is a number of order 1. The total time of the collapse and the final magnitude of core velocities or core radius, depends sensitively on the initial fraction of binaries. For a single mass cluster Heggie, Trenti, & Hut (2006) found that $0.01 \lesssim R_{core}/R_{gc} \lesssim 0.1$, larger values valid for a large frac-

tion of binaries (here R_{gc} is the half-mass radius). In contrast our simple mass segregation led to $R_{50M_{\odot}} = 0.14 R_{gc}$, which is a factor 1.4–14 higher. Note, that the virial theorem implies $v_m \propto R_m$ for a homogeneous mass distribution. Detection rates scale with $R_m^{-3} v_m^{-1}$, and the contribution of $m \sim 50 M_{\odot}$ dominated the final results (see Figs 6 and 7). Therefore post-core collapse mass segregation implies detection rates increased by $(1.4)^4$–$(14)^4$. Thus, in the most optimistic case, we get a substantial increase in the detection rates, i.e. $2.1 \, yr^{-1}$ for InLIGO, $2.8 \, yr^{-1}$ for VIRGO, $6.6 \, day^{-1}$ for AdLIGO, $0.1 \, yr^{-1}$ for LISA, and $4.4 \, hr^{-1}$ for NGLISA!

On the other hand, if core collapse leads to runaway collisions and the buildup of a single intermediate mass black hole, while stellar mass BHs are ejected from the cluster (Freitag, Gürkan, & Rasio 2006), PE detection rates might be considerably suppressed after collapse (i.e. $\nu \propto N_{BH}^2$). More information on the typical properties and long-term evolution of core collapsed clusters is needed to make PE detection rates less uncertain.

7.4. Implications

Opening the gravitational-wave window to observe parabolic encounters of black holes in globular clusters offers a new possibility to constrain BH mass functions and GC models. Since PEs are very sensitive to the number of higher mass stellar BHs (Figs. 6 and 7), our results indicate that a regular detection of PE events would provide accurate limits on the stellar BH mass distribution in GCs. Our analysis shows that this might be possible with AdLIGO if average GCs carry at least 500 BHs.

7.4.1. Galactic Nuclei

The analysis can be extended for other spherically symmetric systems using the scaling $\nu \propto N_{BH}^2 n_{system} v_{vir}^{-1}$. Consider first galactic nuclei, hosting 2500 BHs and approximately all of these BHs have undergone mergers (Portegies Zwart & McMillan 2000). Galactic nuclei abundance in the universe is 100 times less than for GCs (§ 4.2). Assuming that the virial velocity is a factor of $\sqrt{10}$ higher in galactic nuclei and that the CO mass function has the same distribution as in GCs, we get detection rates $\nu^{gal} = 5^2 \times 1/100 \times 1/\sqrt{10} \times \nu^{gc}$. However, the large number of BH mergers likely increases BH masses in galactic nuclei. For a uniform distribution (i.e. $p = 0$) of $N_{BH} = 2500$ between $m_{min} = 80$ and $m_{max} = 100 M_{\odot}$ we get $2500^2/[500 \times (100-80)/(100-5)]^2 \times 1/(100\sqrt{10}) = 1.8$ times the rates shown in the corresponding row of Tab. 1 for GCs: $4. \times 10^{-4} \, yr^{-1}$ for InLIGO, 2.1×10^{-3} for VIRGO, $0.61 \, yr^{-1}$ for AdLIGO, and $5.2 \times 10^{-6} \, yr^{-1}$ for LISA. These numbers should only be regarded as rough estimates, since they result from the direct application of simplified GC model assumptions to galactic nuclei. The calculation assumed uncorrelated two-body interactions which does not hold for motion in the potential of galactic centers (Rauch & Tremaine 1996).

7.4.2. Primordial Black Holes in Galaxies

For a second example consider the GW detections from galactic haloes comprised of low-mass primordial BHs (PBHs) (see e.g. LIGO Scientific Collaboration 2005b and references therein). For a quick upper-limit estimate on the PE detection rate we repeat our analysis for GCs by changing the model parameters to describe galactic haloes. We assume $N_{PBH} = 10^{11}$ PBHs within a maximum radius $R = 5 \, kpc$, a virial

velocity $v_{vir} = 220$ km/s, and a uniform distribution of masses between $m_{min} = 0.25 M_\odot$ and $m_{max} = 0.95 M_\odot$. The maximum distance of a matched filtering detection at a characteristic frequency of $0.9 f_{M\,max} = 4260$ Hz with angular-averaged signal-to-noise ratio $S/N = 5$ is 0.33, 0.62, 4.5, 0, and 0.06 Mpc for InLIGO, VIRGO, AdLIGO, *LISA*, and *NGLISA*, respectively. The final result for the detection rate after the compilation of the full analysis described in the paper gives $\nu = 1.5 \times 10^{-11}$, 1.6×10^{-11}, 2.9×10^{-10}, 2.6×10^{-11}, and 1.4×10^{-9}, respectively. These numbers are comparable to the total NS–NS PE rate in GCs. It is 9 orders of magnitudes smaller than the event rates estimates for PBH binary coalescence in one Milky Way sized galaxy (Ioka et al. 1998; LIGO Scientific Collaboration 2005b).

7.4.3. *Unresolved Parabolic Encounter Background*

Another extension of the present analysis is to estimate the number of low S/N PE events, adding an unresolved astrophysical background to the GW detector noise budget similar to the unresolved WD background (e.g. Hils, Bender, & Webbink 1990; Nelemans, Yungelson, & Portegies Zwart 2001; Benacquista, DeGoes, & Lunder 2004; Cornish & Crowder 2005) and unresolved capture sources (Barack & Cutler 2004b). Since PE rates are progressively larger for progressively smaller characteristic frequencies, f_0, and since all PE waveforms extend to GW frequencies $f \lesssim f_0$, PE background will be most substantial for space detectors, especially around the minimum frequency noise wall ($f_{min} = 10^{-5}$–10^{-4} Hz). The total number of PE events within a distance D, can be obtained from (19) neglecting cosmology as

$$R = \frac{4\pi}{3} D^3 n^{gc} \int_{f_{min}}^{f_{max}} d\nu^{II} \approx 2\pi D^3 n^{gc} \nu_1^{II} \left(\frac{f_{min}}{f_{100}} \right)^{-2/3} \tag{43}$$

where f_{max} is the maximum frequency for PEs avoiding a collision (32), which drops out to leading order if $f_{min} \ll f_{max}$. For $D = 10$ Gpc and $f_{min} = 10^{-5}$ Hz (10^{-4} Hz) we get one event every $1/R = 19$ sec (88 sec), which corresponds to $k = 5300$ (110) events for a 10^{-5} Hz (10^{-4} Hz) frequency bin. If core contraction enhances PE rates by a factor of 14^4 (see § 7.3.3), we get $k = 2 \times 10^8$ (4×10^6) events per frequency bin.

These events will typically have a very low signal-to-noise ratio, e.g. for a single PE encounter with $f_0 = 10^{-5}$ Hz for $m_1 = m_2 = 50 M_\odot$ at $d_L = 10$ Gpc we get $(S/N)_1 \sim 8 \times 10^{-9}$, and $f_0 = 10^{-4}$ Hz yields $(S/N)_1 \sim 2 \times 10^{-7}$ for *LISA*. Assuming that average unresolved PE noise accumulates proportional to $\sqrt{k}$, we get a net amplitude of only $(S/N)_{net} = 10^{-4}$ or 5×10^{-4} for *LISA* even in the core contracted case for frequencies 10^{-5} Hz or 10^{-4} Hz, respectively. Thus, we anticipate that the unresolved PE background adds a negligible amount to the *LISA* noise, and the unresolved PE background from stellar BH encounters will not be an issue for near-future extensions either.

APPENDIX

APPROXIMATE ANALYTICAL FORMULAE

The integrals given in Eq. (19) can be carried out analytically as a Taylor-expansion with respect to the small quantities $\kappa_{BH} = m_{min}/m_{max}$ and $\kappa_{NS} = m_{NS}/m_{max}$. The PE event rate is calculated in three parts

$$\nu_1^{II} = \nu_{1,BH-BH}^{II} + \nu_{1,BH-NS}^{II} + \nu_{1,NS-NS}^{II}, \tag{A1}$$

where $\nu_{1,BH-BH}^{II}$, $\nu_{1,BH-NS}^{II}$, and $\nu_{1,NS-NS}^{II}$ are the event rates of BH-BH, BH-NS, and NS-NS encounters. Substituting the mass dependence in Eq. (19) we get,

$$\nu_1^{II}(m_1, m_2) = \frac{G^{4/3}}{(4\pi)^{2/3}} \frac{N_{CO}^2}{R_{gc}^3 v_{vir}} \frac{(m_1+m_2)^{4/3} m_>^{3/2}}{(m_1^{-1}+m_2^{-1})^{1/2}} f_{100}^{-2/3}, \tag{A2}$$

$$\nu_2^{II}(m_1, m_2) = \frac{2^{1/3} G^{2/3}}{3\pi^{4/3}} \frac{N_{CO}^2 v_{vir}}{R_{gc}^3} (m_1+m_2)^{4/3} (m_1^{-1}+m_2^{-1})^{1/2} m_>^{3/2} f_{100}^{-4/3}. \tag{A3}$$

We approximate the $g_{NS}(m)$ distribution with a Dirac-δ function. Expanding the integrals in Taylor-series in κ_{BH} and κ_{NS}, we get

$$\nu_{1,BH-BH}^{II} = 2^{-4/3} \frac{9}{187} \left(2^{5/6} + \frac{3}{5} \right) \left(1 + 2\kappa_{BH} + 1.364\kappa_{BH}^2 \right) \left(\frac{\langle m_{BH} \rangle}{M_\odot} \right)^2 \left(\frac{m_{max}}{m_{CO}} \right)^{4/3} \nu_1^I, \tag{A4}$$

$$\nu_{1,NS-BH}^{II} = 2^{-1/3} \frac{3}{16} \left(1 + \kappa_{BH} - \kappa_{BH}^{4/3} + \frac{10}{3}\kappa_{NS} + \frac{10}{3}\kappa_{BH}^{1/3}\kappa_{NS} \right) \left(\frac{\langle m_{BH} \rangle}{m_{CO}} \right)^{4/3} \left(\frac{m_{max}}{\langle m_{BH} \rangle} \right)^{1/3} \left(\frac{m_{NS}}{M_\odot} \right)^2 \nu_1^I, \tag{A5}$$

$$\nu_{1,NS-NS}^{II} = 2^{-5/2} \left(\frac{m_{CO}}{M_\odot} \right)^{-4/3} \left(\frac{m_{NS}}{M_\odot} \right)^3 \nu_1^I, \tag{A6}$$

where ν_1^I is the Model-I event rate given by Eq. (17).

Next we present ready-to-use formulas for calculating the detection rates of PEs. Assuming a constant density of GCs, no cosmological and no general relativistic corrections, the detection rate per logarithmic frequency bin becomes

$$\frac{d\nu^{tot}}{d\ln(f_0)} = k \frac{(2GM_\odot)^{19/3}}{c^{12}} n^{gc} N_{CO}^2 R_{gc}^{-3} v_{vir}^{-1} f_0^{4/3} \left(\frac{W(f_0)}{S/N} \right)^3 K(f_0, \lambda) \tag{A7}$$

where S/N is the minimum signal-to-noise ratio (which is set equal to 5 in our numerical results above), $k \equiv 85^{3/2}2^{1/3}\pi^{7/3}/6144 = 2.323$ is a constant coefficient, $v_{\rm vir}$ is the virial velocity (9), $n^{\rm gc}$ is the average GC density in the universe, $R_{\rm gc}$ is the typical radius of the GC, $N_{\rm CO}$ is the number of COs in the GC, $K(f_0, \lambda)$ and $W(f_0)$ are dimensionless terms, $K(f_0, \lambda)$ depending on the CO mass distribution, $g_{\rm CO}$, and $W(f_0)$ on the normalized GW energy spectrum $F(f/f_0)$ Eq. (5), and the detector spectral noise density, $S_n(f)$:

$$K(f_0, \lambda) = \int\int_{f_0 \leq f_{0,\max}[{\rm M}_\odot(x_1+x_2),\lambda]} {\rm d}x_1 {\rm d}x_2\, g_{\rm CO}(x_1)g_{\rm CO}(x_2)\frac{(x_1x_2)^{7/2}x_>^{3/2}}{(x_1+x_2)^{1/6}}, \tag{A8}$$

$$W(f_0) = \sqrt{\frac{4}{5}\int_{f_{\min}}^{f_{\max}}\frac{1}{f^2}\frac{F(f/f_0)}{S_n(f)^2}\,{\rm d}f}. \tag{A9}$$

In terms of f_0, $K(f_0, \lambda)$ is constant for $f_0 \leq f_{0,max}(2m_{\min}, \lambda)$, decreases monotonically for larger f_0 and attains 0 for $f_0 \geq f_{0,\max}(2m_{\max}, \lambda)$ (see Eq. [33] for the definition of $f_{0,\max}(M, \lambda)$, and $m_{\min}$ and $m_{\max}$ are the minimum and maximum masses of the COs, respectively). In Eq. (A8), the integration variables x_1 and x_2 are the dimensionless masses of the COs, for which $m_{\min}/{\rm M}_\odot \leq x_{1,2} \leq m_{\max}/{\rm M}_\odot$. For core collapsed clusters ${\rm M}_\odot$ has to be changed to $m_{\rm core}$, the typical mass of individual components in the core, $R_{\rm gc}$ has to be changed to $R_{\rm core}$, and $v_{\rm vir}$ to $v_{\rm core}$. These values should be set consistently with the core velocity dispersion and core radius which are input parameters for a globular cluster model. For given m components, the velocity dispersion is then $v_m = (m/m_{\rm core})^{-1/2}v_{\rm core}$ and maximum radius from the cluster center is $R_m = (m/m_{\rm core})^{-1/2}R_{\rm core}$.

The total detection rate of parabolic encounters (again assuming a constant density of GCs and no cosmological and general relativistic corrections) is

$$\nu^{\rm tot} = k\frac{(2Gm_{\rm core})^{19/3}}{{\rm c}^{12}}(S/N)^{-3}n^{\rm gc}N_{\rm CO}^2R_{\rm core}^{-3}v_{\rm core}^{-1}\int_{f_{\min}/10}^{f_{0,\max}(2M_{\max}, \lambda)}{\rm d}f_0\,f_0^{1/3}W(f_0)^3K(f_0, \lambda). \tag{A10}$$

REFERENCES

Abbott, B. et al. 2004, Nucl. Instrum. Methods A, 517
Abbott, B. et al. 2005, Phys. Rev. D, 72, 042002
Abbott, B. et al. 2005, Phys. Rev. Lett., 94, 181103
Acernese, F. et al. 2005, Class. Quant. Grav., 22, S869
Ando, M. et al., the TAMA Collaboration, 2005, Class. Quant. Grav., 22, S881
Anninos, P., Hobill, D., Seidel, E., Smarr, L., & Suen W. 1993, Phys. Rev. Lett., 71, 182851
Baker, J. G., Centrella, J., Choi, D., & van Meter, J. 2006, gr-qc/0602026
Barack, L. & Cutler, C. 2004a, Phys. Rev. D, 69, 082005
Barack, L. & Cutler, C. 2004b, Phys. Rev. D, 70, 122002
Binney, J., & Tremaine, S. 1987, Galactic Dynamics (Princeton: Princeton Univ. Press)
Belczynski, K., Sadowski, A., Rasio, F. A., & Bulik, T. 2005, ApJ, submitted, astro-ph/0508005
Benacquista, M. J., DeGoes, J., & Lunder, D. 2004, Class. Quant. Grav., 21, 509
Blanchet, L. & Schäfer 1989, MNRAS, 239, 845
Blanchet, L., Damour, T., Iyer, B. R., Will, C. M., & Wiseman, A. G. 1995, Phys. Rev. Lett., 74, 3515
Blanchet, L., Damour, T., Esposito-Farèse, & Iyer, B. R. 2005, Phys. Rev. D, 71, 124004
Blecha L., Ivanovna, N., Kalogera, V., Belczynski, K., Fregeau, J., & Rasio, F. 2005, ApJ, submitted, astro-ph/0508597
Cardoso, V. & Lemos, J. P. 2003, Phys. Rev. D, 67, 08005
Casares, J. 2005, The Many Scales of the Universe - JENAM 2004 Astrophysics Reviews, Kluwer Academic Publishers, astro-ph/0503071
Chandar, R., Whitmore, B., Lee, M. G. 2004, ApJ, 611, 220
Cutler, C., Kennefick, D., & Poisson, E. 1994, Phys. Rev. D50, 3816
Cornish, N. J. & Crowder, J. 2005, Phys. Rev. D, 72, 043005
Crowder, J. & Cornish, N. J. 2005, Phys. Rev. D, 72, 083005
Cutler, C., & Thorne, K. S. 2002, Proceedings of 16th international conference on General relativity and Gravitation (Eds N.T. Bishop and S.D. Maharaj) (2002); gr-qc/0204090
Davis, M., Ruffini, R., Press, W. H., & Price, R. P. 1971, Phys. Rev. Lett., 27, 1466
D'Eath, P. D., & Payne, P. N., 1992, Phys. Rev. D, 46, 02694
DeSalvo, R. 2004, Class. Quant. Grav., 21, S1145
Djorgovski, S., & Meylan, G. 1994, AJ, 108, 1292
Dymnikova, I. G., Popov, A. K., & Zentsova, A. S. 1982, Ap&SS, 85, 231
Eisenstein, D. J. 1997, astro-ph/9709054
Farouki, R. T., & Salpeter, E. E. 1982, ApJ, 253, 512
Flanagan, É. É. & Hughes, S. A. 1998, Phys. Rev. D, 57, 8
Freitag, M. 2003, ApJ, 583, L21

Freitag, M., Gürkan, M. A., & Rasio, F. A. 2006, MNRAS, in press, astro-ph/0503130
Fryer, C. L. & Kalogera, V. 2001, ApJ, 554, 548
Gair, J. R., Barack, L., Creighton, T., Cutler, C., Larson, S. L., Phinney, E. S., & Vallisneri, M. 2004, Class. Quant. Grav., 21, 1595
Gair, J. R., Kennefick, D. J., & Larson, S. L. 2005, Phys. Rev. D, 72, 084009
Gair, J. R., Kennefick, D. J., & Larson, S. L. 2006, ApJ, in press, astro-ph/0508275
Gebhardt K., Rich, R. M., & Ho, L. C. 2005, ApJ, 634, 1093
Grote, H. et al. 2005, Class. Quant. Grav., 22, S193
Goudfrooij, P., Strader, J., Brenneman, L., Kissler-Patig, M., Minniti, D., & Edwin Huizinga, J. 2001, MNRAS, 343, 665
Gültekin, K., Miller, M. C., & Hamilton, D. P 2006, ApJ, in press, astro-ph/0509885
Gürkan, M. A., Freitag, M., & Rasio, F. A. 2004, ApJ, 604, 632
Heggie, D. C., Trenti, M., & Hut, P. 2006, astro-ph/0602408
Hills, J. G., & Day, C. A. 1976, Astrophys. Lett., 17, 87
Hils, D., Bender, P. L., & Webbink, R. F. 1990, ApJ, 360, 75
Hopman, C., & Alexander, T. 2005, ApJ, 629, 362
Hopman, C., & Portegies Zwart, S. 2005, MNRAS, 363, L56
Hughes, S. A., Márka, S., Bender, P. L., & Hogan, C. J. 2001, Proc. of the APS/DPF/DPB Summer Study on the Future of Particle Physics (Snowmass 2001) ed. Graf, N. eConf, C010630, 402, astro-ph/0110349
Ioka, K., Chiba, T., Tanaka, T., & Nakamura, T. 1998, Phys. Rev. D, 58, 063003
Jaronowski, P., Kokkotas, K. D., Królak, A., & Tsegas, G. 1996, Class. Quantum Grav., 13, 1279
Kalogera, V. et al. 2004, ApJ, 601, L179
Khanna, G., Baker, J., Gleiser, R. J., Laguna, P., Nicasio, C. O., Nollert, H., Price, R., & Pullin, J. 1999, Phys. Rev. Lett., 83, 3581
Kocsis, B. & Gáspár, M. E. 2004, LIGO note, http://www.ligo.caltech.edu/docs/T/T030136-00.pdf
Kovács, S. J., & Thorne, K. S. 1978, ApJ, 224, 62
Kroupa, P., & Weidner, C. 2003, ApJ, 598, 1076
Lazzarini, A., & Weiss, R. 1996, LIGO note, http://www.ligo.caltech.edu/docs/E/E950018-02.pdf
Lee, M. H. 1993, ApJ, 418, 147
LIGO Scientific Collaboration, 2005a, Phys. Rev. D, 72, 062001
LIGO Scientific Collaboration, 2005b, Phys. Rev. D, 72, 082002
Lipunov, V. M., Postnov, K. A., & Prokhorov, M. E. 1997, NewA, 2, 43
Lotz, J. M., Miller, B. W., Ferguson, H. C. 2004, ApJ, 613, 262
Martel, K. 2004, Phys. Rev. D, 69, 044025
Meylan, G. 1987, A&A, 184, 144
Mikóczi, B., Vasúth, M., & Gergely, L. Á. 2005, Phys. Rev. D, 71, 124043
Miller, M. C. 2002, ApJ, 581, 438

Miller, M. C. & Colbert, E. J. M. 2004, Int'l J. of Mod. Phys. D, 13, 1, 1

Misner, C. W., Thorne, K. S., & Wheeler, J. A. 1973, Gravitation (San Francisco: Freeman)

Mine, Y., Shibata, M., & Tanaka, T. 1996, Phys. Rev. D, 53, 020622

Moreschi, O. M. 1999, Phys. Rev. D, 59, 084018

Nakar, E., Gal-Yam, A., & Fox, D. B. 2005, ApJ, submitted, astro-ph/0511254

Nelemans, G., Yungelson, L. R., & Portegies Zwart, S. F. 2001, A&A, 375, 890

O'Leary, R. M., Rasio, F. A., Fregeau, J. M., Ivanova, N., & O'Shaughnessy, R. 2006, ApJ, 637, 937

Portegies Zwart, S. F., Baumgardt, H., McMillan, S. L. W., Makino, J., Hut P., & Ebisuzaki, T. 2006, ApJ, in press, astro-ph/0511397

Portegies Zwart, S. F. & McMillan, S. L. W. 2000, ApJ, 528, 17

Portegies Zwart, S. F. & Spreeuw, H. N. 1996, A&A, 312, 670

Portegies Zwart, S. F. & Yungelson, L. R. 1998, A&A, 312, 670

Postnov, K. A. & Prokhorov, M. E. 2001, Astr. Rep., 45, 899

Price, R. H., & Pullin, J. 1994, Phys. Rev. Lett., 72, 3297

Pryor, C., & Meylan, G. 1993, in ASP Conf. Ser. 50, Structire and Dynamics of Globular Clusters, ed. S. G. Djorgovski & G. Meylan (San Fransisco: ASP), 357

Ptak, A., & Colbert, E. 2004, ApJ, 606, 291

Rauch, K. P., & Tremaine, S. 1996, New Astronomy, 149

Saslaw, Gravitational physics of stellar and galactical systems, 1985, Cambridge Univ. Press, 52

Sasaki, M. & Nakamura, T. 1982, Prog. Tbeor. Phys., 67, 1788

Scalo, J. M. 1986, Fundam. Cosmic Phys., 11, 1

Seto, N., Kawamura, S., Nakamura, T. 2001, Phys. Rev. Lett., 87, 221103

Sigurdsson, S., & Hernquist, J. 1993, Nature, 364, 423

Sigurdsson, S., & Phinney, E. S. 1995, ApJS, 99, 609

Sigurdsson S., & Rees, M. J. 1997, MNRAS, 284, 318

Sperhake, U., Kelly, B., Laguna, P., Smith, K. L., & Schnetter E. 2005, Phys. Rev. D, 71, 124042

Spitzer, L., Jr. 1969, ApJ, 158, L139

van den Bergh, S. 2005, ApJ, submitted, astro-ph/0509811

Tegmark, M. et al. 2004, Phys. Rev. D, 69, 103501

Timpano, S., Rubbo, L. J., & Cornish, N. J. 2005, gr-qc/0504071

Thorne, K. S. 1987, in 300 Years of Gravitation, ed. Hawking, S. W. & Israel, W., Cambridge University Press, pp. 330 – 458

Tully, R. B. 1988, AJ, 96, 73

Turner, M. 1977, ApJ, 216, 610

Watters, W. A., Joshi, K. J., & Rasio, F. A. 2000, ApJ, 539, 331

Will, C. M. 2004, ApJ, 611, 1080